Therapeutic potential of USP14 and UCHL5 mediated ERRα regulation to control mitochondrial function in pancreatic cancer

Jae Woong Jeong

The Graduate School
Yonsei University
Department of Medicine

Therapeutic potential of USP14 and UCHL5 mediated ERRα regulation to control mitochondrial function in pancreatic cancer

A Dissertation Submitted
to the Department of Medicine
and the Graduate School of Yonsei University
in partial fulfillment of the
requirements for the degree of
Doctor of Philosophy in Medical Science

Jae Woong Jeong

December 2024

This certifies that the Dissertation of Jae Woong Jeong is approved

Thesis Supervisor Sungsoon Fang

Thesis Committee Member Cheol Ryong Ku

Thesis Committee Member Joon Seong Park

Thesis Committee Member Jinhyuk Bhin

Thesis Committee Member Hyunkyung Kim

The Graduate School
Yonsei University
December 2024

ACKNOWLEDGEMENTS

First of all, I would like to express gratitude to my advisor, Prof. Sungsoon Fang, for his guidance and enthusiasm throughout my degree program. His encourageful advice and experienced research guidance have led me to where I am today. I would like to thank him again for inspiring and motivating me over the years.

I am deeply grateful to the members of my thesis committee, Prof. Cheol Ryong Ku, Prof. Joon Seong Park, Prof. Hyunkyung Kim and Prof. Jinhyuk Bhin. Their insightful feedback and support contributed greatly to the logic and coherence of my dissertation.

My committee chairman, Prof. Cheol Ryong Ku, has always been supportive throughout meetings with constructive guidance and provided invaluable suggestions to improve my research. Prof. Joon Seong Park's insights as a Hepato-Biliary-Pancreatic Surgery clinician and his provision of clinical data have been invaluable in helping me to validate the assumptions of this dissertation. Prof. Hyunkyung Kim’s continuous and enthusiastic guidance has been indispensable in helping me navigate and complete my degree journey. Prof. Jinhyuk Bhin’s expertise in bioinformatics has provided the technical knowledge necessary to effectively integrate bioinformatics into my study.

I also would like to express to my colleagues, Dr. Nahee Hwang, Dr. Hyeonhui Kim, Dr. Yeseong Hwang, Dr. Minki Kim, Sugyeong Jo,

Seyeon Joo, Chae Min Lee, Ye-Chan Park. To all of you, I sincerely thank you for your support, help, and guidance throughout my graduate academic life. Each of you has contributed in meaningful ways, from thoughtful discussions to simply being there during challenging moments. I am sincerely grateful for the camaraderie and intellectual engagement we shared.

I would also like to express my deepest gratitude to my family. To my parents, who have always been there for me, offering unwavering emotional support and dedication throughout every step of my journey—your love has been my greatest source of strength. To my sister and brother-in-law, who have steadfastly supported and uplifted me, you have provided the backbone that helped me reach this milestone. I truly believe that my family is the foundation of who I am today, and I am forever grateful for everything you've done for me.

Lastly, I want to express sincere appreciation to my wife, Hyobin An. Your support and love have been a tremendous motivation during my degree course. I would not have been able to complete this journey without you. Thank you always, and I love you dearly.

TABLE OF CONTENTS

LIST OF FIGURES

ABSTRACT

Therapeutic potential of USP14 and UCHL5 mediated ERRα regulation to control mitochondrial function in pancreatic cancer

Pancreatic ductal adenocarcinoma (PDAC), majority subtype of pancreatic cancer, is lethal disease showing a five-year survival rate of about 10%. The rapid proliferation and metabolic characteristic of PDAC require an increased protein turnover rate, leading proteotoxic stress. The high proteasome activity of PDAC makes it a promising target for therapeutic target for PDAC. Two proteasomal deubiquitinases, Ubiquitin specific peptidase 14 (USP14) and Ubiquitin carboxyl-terminal hydrolase isozyme L5 (UCHL5), act as ubiquitin-trimmer on substrates. Interestingly, analysis of PDAC sequencing data showed that aggressive ductal cells exhibited high expression levels of USP14 and UCHL5, which correlated with poor patient survival rate. It was verified by mutiple sequencing analysis and immunohistochemistry assay.

To address USP14 and UCHL5 as potential therapeutic targets, this study investigated what phenotypic changes of PDAC cell lines exhibited after treatment with b-AP15, a specific dual inhibitor of USP14 and UCHL5. As expected, b-AP15 treatment showed significant proliferation inhibition in PDAC cell lines and even xenograft models, suggesting potential therapeutic efficacy. To elucidate mechanisms of cellular phenotypic changes to faster cell growth, transcriptomics and proteomics were employed. These comprehensive analyses revealed that a critical impact on mitochondrial function in PDAC cells. Importantly, the data indicated a inhibition of oxidative phosphorylation through estrogen-related receptor alpha autophagical degratation. These findings suggest the potential of b -AP15 as a therapeutic strategy targeting PDAC.

Key words: Pancreatic ductal adenocarcinoma, USP14, UCHL5, ERRα, oxidative phosphorylation

1. INTRODUCTION

Pancreatic cancer is a mortal disease with the five-year survival rate of 13% in 2024[1]. Despite accounting for only 3% of all cancer cases, pancreatic cancer is the third leading cause of cancer death[1]. If these trends persist, it is projected to become the second leading cause of death by 2030[2]. Pancreatic ductal adenocarcinoma (PDAC) is the dominant subtype of pancreatic cancer presenting about 90% of cases[3,4]. The cancer cells of PDAC originate from aggresiveness of pancreatic ductal epithelial cell[5], presenting high somatic mutation rate of KRAS, P53, CDKN2A and SMAD4[6-8]. The genetic changes of PDAC cells induce uncontrol of proliferation along with supression of immunity by tumor microenviroment[9]. Due to the critical danger of PDAC to patients, developing effective strategies to address this disease is essential.

The therapeutic approaches to PDAC include surgical procedures such as the pancreaticoduodenectomy[10], radiotherapy[11] and chemotherapy[12]. The chemotherapy regimens involve gemcitabine, 5-fluorouracil, the FOLFIRINOX protocol, erlotinib and nab-paclitaxel[12]. The most chemotherapies target mechanisms of cell cycle inhibition. However, the emergence of regimen resistance remain a challenging point in PDAC therapy[13].

Ubiquitin-proteasome system (UPS) is a cellular process of controlling proteasomal degradation of ubiquitinated protein. Ubiquitin ligation to lysine residues on proteins by E1, E2 and E3 equips the proteins with diverse functions[14], called ubiquitination. K48-linked ubiquitin, for example, is known to induce proteasomal degradation of substrate proteins. The proteasome is a major player in proteolysis, composed of two 19S regulatory particles and 20S core particle[15]. The 19S regulatory particle, lid part of proteasome, recognizes polyubiquitin chains of recreuited substrates by ribophorin 1 (RPN1), ribophorin 10 (RPN10) and ribophorin 13 (RPN13), and deubiquitinase them by proteasomal deubiquitinases, USP14 and UCHL5. Specifically, USP14 and UCHL5 cleave polyubiquitin chains of substrates[16]. A crucial function of USP14 and UCHL5 is the recycle of detached ubiquitins from substrates into the cytoplasmic free ubiquitin pool [17,18]. Then the remained substrates are entered to 20S core particles, consisting of ring structure which degrades the substrate.

Proteostasis, a protein homeostasis, refers to the regulation of the protein turnover cycle including protein synthesis, folding, conformational stability and degradation[19]. As exprected the cancer cells are highly rely on proteostasis mechanism due to factors such as mutant and overexpressed proteins[20].

To address proteostasis imbalance, the cancer cells require a increased UPS and chaperone activity[21,22]. Bortezomib[23], Carfilzomib[24] and Ixazomib[25], currently FDA-approved proteasome inhibitors, have an inhibition mechanism by targetting the 20S core particle. These proteasome inhibitors have applications in hematologic cancer therapy such as multiple myeloma and mantle cell lymphoma[23-25]. Encouragingly, they are being actively investigated in solid tumors, such as colorectal[26], gastric[27], prostate cancer[28], and breast cancer[29]. Interestingly, it has been suggested that the proteasome activity is a necessary for initiating Pancreatic Intraepithelial Neoplasia (PanIN)[30], the histological precursor of PDAC[31]. Given the increased proteasome activity in cancer cells[21], these researches highlight the proteasome as a promising target for potential PDAC therapy.

Here I hypothesized that the function of USP14 and UCHL5 increased in parallel with proteasome activity in PDAC cells, and aimed to apply both proteins as proteasome controllers to PDAC. To investigate the clinical potential significance of USP14 and UCHL5 in PDAC, published transcriptomic data were employed, including the bulk RNA sequencing (bulk RNA-seq), single cell RNA sequencing (scRNA-seq) and spatial single cell RNA sequencing (spatial scRNA-seq). The analysis results showed that PDAC patient tissues exhibited increased expression levels of USP14 and UCHL5 compared to normal pancreaic tissues. Additionally, the reverse correlation of both genes expression levels and survival probabilty was demonstrated in Kaplan-Meire assay. The implication of relation between both genes and PDAC aggressiveness was revealed.

Subsequently, b-AP15, the dual specific inhibitor of USP14 and UCHL5[32], was engaged to explore the potential of these proteins as therapeutic targets for PDAC. The small molecule b-AP15 abrogates the proteasomal deubiquitination of the 19S regulatory particles[33]. The b-AP15 compound has been the subject of extensive research with the aim of inducing apoptosis through proteasome inhibition[34-36]. The results of one research have demonstrated that apoptosis occurs as a consequence of the stabilization of death receptor 5 (DR5/TNFRSF10B), the receptor for TNF-related apoptosis-inducing ligand (TRAIL), which is known to induce apoptosis[34]. Nevertheless, no prior studies had previously been conducted on this compound in the context of PDAC. Therefore, in this study, b-AP15 was investigated as a potential novel therapeutic molecule for PDAC.

The administration of b-AP15 significantly inhibited cell growth rate of PDAC cell lines and in vivo xenograft models. Then, the transcriptomic and proteomic analysis was conducted to elucidate the mode of action of b-AP15 on PDAC cell lines, presenting increased proteotoxic stress and oxidative stress, and reduced OXPHOS. Importantly, the protein expression levels of estrogen-

related receptor alpha (ERRα; ESRRA), key site-specific transcription factor of mitochondrial biosynthesis[37-39], was reduced at the b-AP15 treatment conditions. Considering studies targeting mitochondrial complexes in PDAC cells as therapeutic strategies, controlling ERRα using USP14 and UCHL5 is an intriguing mechanism.

In this study, I present cellular phenotypic changes and mechanisms of b-AP15 treatment on PDAC cell lines. Chiefly, the inhibition of both USP14 and UCHL5 reduced cell prolifeation throught diminishing OXPHOS via ERRα autophagic degradation in PDAC, suggesting novel therapeutic potiential targets.

2. MATERIALS AND METHODS

2.1. TCGA pancreatic cancer dataset

To compare the expression levels of USP14 and UCHL5 between PDAC and normal tissues, and perform correlation analysis, merged Pancreatic Adenocarcinoma (PAAD) data set from TCGA and Genotype-Tissue Expression (GTEx) were employed using GEPIA (https://gepia.cancer-pku.cn)[40]. A comparative analysis of the expression levels of USP14 and UCHL5 in normal (n = 171) and PAAD (n = 179) samples was used. For corrleation analysis, PAAD patients (n = 179) samples were utilized with the Pearson statistics.

To investigate clinical implication of USP14 and UCHL5 in PDAC, the sequencing expression data of PAAD (n = 178) was collected using the TCGAbiolinks package (v.2.29.6) in R. Then, data was normalized to Trimmed Mean of M-value (TMM) expression levels using the edgeR pacakge in R. For phenotypic analysis, patients were splited into USP14 ^{High} or USP14 ^{Low} groups and UCHL5 ^{High} or UCHL5 ^{Low} groups based on USP14 and UCHL5 levels. And principal component analysis (PCA) was performed using FactoMineR package (v.2.8) and factoextra package (v.1.0.7) in R. For survival probability analysis, Kaplan-Meier analysis was performed ising clinical data of PAAD.

2.2. Kaplan-Meier analysis

Survival probability analysis was performed using Kaplan-Meier analysis. For PAAD patients, clinical data of TCGA was employed, visualized by GraphPad. And it was validated by additional PDAC data analysis using Kaplan-Meier Plotter database (https://kmplot.com/analysis/).

2.3. Spatial scRNA-seq analysis (Visium)

Spatial scRNA-seq analysis was performed to confirm the expression patterns of USP14 and UCHL5 in aggressive pancreatic ductal cell using three PDAC patients Visium data from GSE211895. The three PDAC patietns data was collected from Gene Expression Omnibus (GEO) and processed using Seurat package (v.4.3.0) in R. PCA was performed to reduce dimensions and Uniform Manifold Approximation and Projection (UMAP) was used to visualized in two-

dimension. Among clusters, cluster with high ductal cell marker genes, *EPCAM* and *TSPAN3*, and prolifeartion marker genes, *MKI67* and *TOP2A* was designated as Cycling Ductal Cells. Patient A for Cluster 2, Patient B for cluster 0, Patient C for Cluster 2. The expression levels of *EPCAM*, *USP14* and *UCHL5* in two-demensions were visualized using spatial feature plot. The spatial plot of *USP14* and *UCHL5* were merged to determine how the two genes are co-expressed and overlap with *EPCAM* expression and the Cycling Ductal cell cluster.

2.4. Immunohistochemistry (IHC) assay

IHC was performed to compared proitein expression levels between normal pancreas and PDAC tissues. Tissue slide was stained using diluted monoclonal specific antibodeis for USP14 (1:100; Santa Cruz Biotechnology, USA) and UCHL5 (1:100; Santa Cruz Biotechnology, USA). After staining, cytoplasmic USP14 and UCHL5 expression was scored as: 0, 1+, 2+ and 3+. For intensity of USP14 and UCHL5, ImageJ (v.1.52a) was used.

2.5. scRNA-seq analysis

To investigate PDAC cancer cells on single cell levels, scRNA-seq analysis was performed using 29 patients PDAC patients scRNA-seq data from GSE154778, GSE155698 and GSE212966. All patients data were collceted from GEO and processed using Seurat package in R. Quality control was processed to select singlets using DoubletFinder package (v.2.0.3) in R and 29 data were integerated to one merged data. The integrated data was performed PCA, visualized by UMAP and identified to 8 clusters based on expression levels of marker genes.

The ductal cell cluster for KRT19, TSPAN3, and SOX9; the acinar cell cluster for CTRC, CTRB1, and PRSS1; the T cell cluster for CD3E, CD3D, and CD8A; the B cell cluster for CD19, MS5A1, and CD79A; the macrophage cluster for CD14, CD163, and CD68; the endothelial cell cluster for CDH5, CLDN5, and PEACAM1; the fibroblast cluster for LUM, COL1A1, and COL5A2; and the mast cell cluster for CPA3, TPSAB1, and TPSB2. Their marker genes were verified using dot pot and feature plot.

For trajectory analysis, pseudotime was estimated using Monocle3 package (v.1.3.1) and slingshot package (v.2.2.1) in R. The independent pseudotime results from two packages were correlated and visualized by feature plot and feature scatter plot. For Gene Set Enrichment Analysis (GSEA), fgsea

pacakge (v.1.27.0) was used. Additionally, single sample GSEA (ssGSEA) was performed using escape package (v.1.4.0).

2.6. Cell culture

Human PDAC cell lines, PANC1 and MIAPACA2 were purchased from American Type Culture Collection (ATCC; USA). The cells were cultured at 10cm culture plate (Falcon) in 5% CO2 incubator at 37°C. Cell was maintained with Dulbecco's Modified Eagle Medium (DMEM; Corning, USA) supplemented with 10% fetal bovine serum (FBS; Corning, USA) and 1% penicillin-streptomycin (Gibco). Cell lines were subcultured at pproximately 70-80% confluency using 0.25% trypsin-EDTA (Gibco, USA).

2.7. Cell proliferation assay

Proliferation rate of PDAC cells was measured using Cell Counting Kit-8 (CCK8; Dojindo, Japan) according to manufacturer's instructions. PDAC cell lines were seeded into 96-well plates (Falcon, USA). Under the experimental conditions specified, 10 μL of CCK-8 solution was added to each well (100 μL). The cells were then incubated at 5% CO2 incubator for 1 hr. Then, absorbance was measured at 450 nm using a microplate reader to assess cell proliferation rate.

2.8. Colony formation assay

To measure coloy formation rate of PDAC cells, crystal violet staining was employed. First, PDAC cells were seeded to 6-well plates (Falcon, USA) and were incubated at 5% CO2 incubator for 10 days. Then, cells were washed using phosphate-buffered saline (PBS; Corning, USA), fixed with methanol, and stained with 0.1% crystal violet for 10 min.

2.9. Wound healing assay

To estimate recovery rate of scratched PDAC cells, wound healing assay was performed. Cells were seeded into 6-well plates, scratched and incubated at 5% CO2 incubator. Then, it was visualized at time points of 0, 24, 48, and 72 hr to measure the recovery rate.

2.10. Cell cycle assay

The ratio of cell cycle phase was estimated by propidium iodide (PI; Invitrogen, USA) staining. Under the experimental conditions specified, PDAC cells were washed with PBS, stained with PI staining solution (35 μg/mL PI, 100 μg/mL RNase A (Thermo Fisher Scientific, USA), and 0.1% Triton X-100 (Amresco, USA)) for 30 min. Flow cytometry data were acquired with BD FACSVerse (BD Biosciences, USA) and collected with BD FACSuite (BD Biosciences, v.1.0.6), analyzed using FlowJo (BD Biosciences, v.10.7.1).

2.11. Tumor xenografts

To validate in vivo analysis using b-AP15, tumor xenograft model was employed. The female BALB/c nude mice were purchased from Orient Bio (South Korea). The nude mice were housed in specific-pathogen-free conditions in individually ventilated cages, under 30–70% humidity, 21–26°C temperature, and a 12-hr light–dark cycle.

Approximately, 1 x 10^6 MIAPACA2 cells resuspended with 1:1 Matrigel (Corning, USA) were injected subcutaneously in the right flank of mice. After 2 weeks, tumor grew to about 100 mm^3, the mice were randomly divided into two groups. Then, each group were intraperitoneally injected with either vehicle (DMSO: PEG400: PBS = 1: 6: 3) or b-AP15 (7.5 mg/kg; b-AP15: PEG400: PBS = 1: 6: 3) for 3 times a week. The tumor volume was calculated following formula: (width^2 x length) x 0.5. After 11 times of injections, the in vivo xenograft models were sacrificed on 26 day before the largest tumor volume of the mouse reached 2000 mm^3. Tumors were removed from sacrificed mouse, photographed, and weighted. All animal experiment was approved by the Institutional Animal Care and Use Committee of Yonsei University College of Medicine (IACUC), according to guidelines by the Association for Assessment and Accreditation of Laboratory Animal Care International (AAALAC International).

2.12. Protein extraction and western blotting

Protein extraction for protein immunoblotting was performed using EBC200 lysis buffer (50 mM Tris-HCl, pH 8.0, 200 mM NaCl, 0.5% NP-40) supplemented with Protease Inhibitor (GenDEPOT, USA). Total cell lysates were centrifuged at 4°C, 13,000 rpm, for 15 min. Then, supernatants were transfer to new tubes and concentration of proteins were estimated using the BCA Protein Assay

kit (Thermo Fisher Scientific, USA). Equal amounts of proteins mixed with 4X Laemmli sample buffer (Bio-Rad, USA) were seqparted by sodium dodecyl sulfate polyacrylamide gel electrophoresis (SDS-PAGE) and transfer to polyvinylidene difluoride (PVDF; Bio-Rad, USA). Subsequently, the PVDF was blocked with 5% skim milk (BD, USA) in tris-buffered saline Tween-20 (TBS-T) for 1h and probed with the primary antibody for overnight. After washing PVDF with TBS-T, it was probed with horseradish peroxidase conjugated secondary antibody and washed with TBS-T. The immunoblots were visualized using enhanced chemiluminescence solution (Bio-Rad, USA).

The primary specific antibodies against ubiquitin (1:2000), and ERRα (1:2000) were purchased from Cell Signaling Technology (USA), against K48-ubiquitin (1:2000) was purchased from Abcam (USA), and against USP14(1:2500), UCHL5 (1:2500), and α-actinin (1:5000) were purchase from Santa Cruz Biotechnology (USA). The horseradish peroxidase conjugated secondary antibodies against mouse IgG (1:10000) was purchased from Cell Signaling Technology (USA), and against rabbit IgG (1:10000) was purchased from Abcam (USA).

2.13. LC/MS (proteomics)

Total protein lysates were transported to ebiogen Inc. (https://www.e-biogen.com). Brieflty, for digestion, the lysates were processed the filter aided saample preparation (FASP) digestion through reducing with 5 mM TCEP, alkylating with 50 mM IAA and digestion using ABC with trypsin. Then, desalting was processed using C18 Micro Spin Column (Thermo Fisher Scientific, USA). Proteomics data was collected was conducted with the desalted samples using UPLC Orbitrap exploris 480 (Thermo Fisher Scientific, USA). Data analysis was processed using Proteome Discoverer (Thermo Fisher Scientific, USA).

2.14. RNA extraction and real-time quantitative PCR

Total RNA was extracted using TRIzol reagent (Invitrogen, USA) according to manufacturer's instructions. Then, cDNA construction was performed using ImProm-II Reverse Transcriptase (Promega, USA). For real-time quantitative PCR was performed using cDNA, TOP Real qPCR 2X Pre-MIX (Enzynomics, Korea) and specific paired primers on a CFX Connect Real-Time PCR System (Bio-Rad, USA). Gene expression was normalized to the 36B4 as housekeeping gene using

ΔΔCt method. The sequences of the primers used in the qPCR are shown below.
36B4 (F: CGTCCTCGTTGGAGTGACA, R: CGGTGCGTCAGGGATTG)
ATF4 (F: CCCTTCACCTTCTTACAACCTC, R: TGCCCAGCTCTAAACTAAAGGA)
DDIT3 (F: GGAAACAGAGTGGTCATTCCC, R: CTGCTTGAGCCGTTCATTCTC)
ATF3 (F: TGCTCAGAGAAGTCGGAAGAA, R: TGGCACAAAGTTCATAGGGCA)
HSPA1A (F: CGGCACTCTGGCCTCTGATT, R: GACCCGCCTTTTCCCTTCTG)
HSPA6 (F: CAAGGTGCGCGTATGCTAC, R: GCTCATTGATGATCCGCAACAC)
DNAJA1 (F: AGGAGCAGTAGAGTGCTGTCC, R: TCTCGAACTATCTTCCTTCCGT)
GPX1 (F: CAGTCGGTGTATGCCTTCTCG, R: GAGGGACGCCACATTCTCG)
GPX4 (F: GAGGCAAGACCGAAGTAAACTAC, R: CCGAACTGGTTACACGGGAA)
GSS (F: TACGGCTCACCCAATGCTC, R: CTATGGCACGCTGGTCAAATA)
HMOX1 (F: AAGACTGCGTTCCTGCTCAAC, R: AAAGCCCTACAGCAACTGTCG)
SOD1 (F: GGTGGGCCAAAGGATGAAGAG, R: CCACAAGCCAAACGACTTCC)
ESRRA (F: AGGGTTCCTCGGAGACAGAG, R: TCACAGGATGCCACACCATAG)
NDUFA2 (F: GCAGCAAGTCGAGGAGTCG, R: CGTTTCTCAATGAAGTCCCTGA)
SDHA (F: CAGCATGTGTTACCAAGCTGT, R: GGTGTCGTAGAAATGCCACCT)
COX8A (F: TTACCTCCTGCTTCGTGACC, R: CACTCTGGCCTCCTGTAGGT)

2.15. Bulk RNA-seq (transcriptomics)

Extracted total RNA was transported to Macrogen Inc. (https://dna.macrogen.com). Briefly, the libraries were constructed using TruSeq Stranded mRNA Library Prep Kit (Illumina, USA) according to manufacturer's instructions. Then, sequencing was performed on NovaSeq6000 (Illumina, USA) platform using a NovaSeq 6000 S4 Reagent Kit (Illumina, USA). Raw sequencing data, FASTQ file, were qulitified using FastQC (v0.11.7), trimmed using Trimmomatic (v.0.38), mapped using HISAT2 (v.2.1.0) and Bowtie2 (v.2.3.4.1), and assembled using StringTie (v.2.1.3.b). The raw count expression value was subjected to TPM normalization. The normalized expression values were used to calculate differential expression genes (DEGs), conducted using edgeR package.

2.16. Immunoprecipitation (IP) assay

Proteins extracted from cell lines were quantified using a BCA assay after lysis. Approximately 10% of the total protein extract was collected, mixed with 4X Laemmli sample buffer and boiled at 100°C for 5 min. The remaining protein samples were precleared with sepharose beads (CL4B 2: Protein A 1: Protein G 1; Cytiva, USA) to limit unspecific binding of IgG. The precleared protein samples were incubated overnight with antibody specific for ERRα or IgG on a rotator at 4°C. Then samples were incubated with sepharose beads for 1 h on a rotator at 4°C. After that, they were washed with EBC 200 lysis buffer. 2X Laemmli sample buffer diluted from 4X Laemmli sample buffer were mixed with washed samples and boiled. These boiled samples were subjected to SDS-PAGE, transferred onto membranes, and visualized using western blotting as previously described

2.17. ROS analysis

Cellular reactive oxygen species (ROS) levels were estimated using DCFDA/H2DCFDA – Cellular ROS Assay Kit (Abcam, USA) according to manufacturer's instructions. Under the experimental conditions specified, cells were stained with 10 μM DCFDA into 96-well black plates (Falcon, USA). Then, ROS data was evaluated using a fluorometer with an excitation wavelength of 485 and emission wavelength of 535 nm.

2.18. Oxidized protein assay

Oxidized protein assay was conducted using Oxidized Protein Western Blot Detection Kit (Abcam, USA) according to manufacturer's instructions. Briefly, protein lysates were extracted using Extraction Buffer and concentration of proteins were evaluated using the BCA Protein Assay kit. Then, equal amounts of proteins were incubated with sodium dodecyl sulfate (SDS) and 2,4-Dinitrophenylhydrazine (DNPH) Solution for 15 min at room temperature, and samples were added Neutralization Solution. The samples were processed western blotting assay with 5000X Primary anti-DNP Antibody and 5000X HRP Conjugated Secondary Antibody.

2.19. Luciferase assay

Luciferase assay was conducted to assess the activity of the estrogen-related receptor response

element (ERRE) motif (sequence: TCAAGGTCA), binding sequence of ERRα, using ERRE promoter luciferase reporter plasmid (3xERRE-luciferase; Addgene, USA) and β-galactosidase plasmid. Lipofectamine 3000 transfection reagent (Invitrogen, USA) was used to transfect the plasmids into cells. Protein extraction was used luciferase lysis buffer (12.5% Glycerol (Thermo Fisher Scientific, USA), 5 mM CDTA (Millipore, USA), 12.5 mM Trisphosphate (Tris, Bio-Rad, USA; Phosphoric acid, Sigma, USA), 0.1% Triton-X100 (Amresco, USA), 1 mM Dithiothreitol (TCI, Japan) and seeded into 96-well white plates (SPL, Republic of Korea). Luciferase activity was measured with Microplate luminometer (EG&G, USA) using Luciferase Buffer (90 mM KPO4 (SAMCHUN, Republic of Korea), 10 mM MgCl2 (Sigma, USA), 20 mM ATP (TCI, Japan), 0.5 mM D-luciferin (Promega, USA) and β-galactosidase activity was assessed with absorbance of 420 nm using ONPG Buffer (51 mM NA2HPO4 (SAMCHUN, Republic of Korea), 34 mM NAH2PO4 (Amresco, USA), 1 mM MgCl2, 1 mM ONPG (Sigma, USA). The ERRE activity was normalized to β-galactosidase activity.

2.20. Chromatin Immunoprecipitation (ChIP) assay

ChIP assay was conducted to assess the activity between ERRα and the its binding site, ERRE, around mitochondrial genes. First, cells were fixed with 16% Formaldehyde (Thermo Fisher Scientific, USA) for cross-linking. 125 mM glycine (Amresco, USA) was added to quench the cross-linking. Then, nuclear extraction was performed with Nuclear Lysis Buffer (150 mM NaCl, 50 mM Tris-HCl, 5 mM EDTA, 0.5% NP-40). Sonication was conducted with Sonication Buffer (10 mM EDTA, 50 mM Tris-Hcl) supplemented SDS using Covaris M220 (USA). The sheared sampels were diluted with Dilution Buffer (1% Triton X-100, 2 mM EDTA, 150 mM NaCl, 20 mM Tris-HCl) and incubated with antibodies at 4°C for overnight using rotater. Sepharose beads were used to bind antibodies and washed with TSE buffers (TSE1: 0.1% SDS, 1% Triton X-100, 2 mM EDTA, 20 mM Tris-HCl and 150 mM NaCl; TSE2: 0.1% SDS, 1% Triton X-100, 2 mM EDTA, 20 mM Tris-HCl and 500 mM NaCl), 3rd Wash buffer (0.25 M LiCl, 1% NP-40, 1% deoxycholate, 1 mM EDTA and 10 mM Tris-HCl) and TE buffer (1 mM EDTA and 10 mM Tris-HCl). DNA was eluted using Elution buffer (1% SDS, 50 Mm EDTA and 50 mM Tris-HCl) supplemented with 1 µl Proteinase K (20µg/µl) and samples were incubated at 65 °C for overnight to perfrorm reverse-crosslinking. The eluted DNA was purified using QIAquick PCR Purification Kit (QIAGEN, Germany). Subsequently, qPCR was conducted using purified DNA.

CYTB (F: GCCTGCCTGATCCTCCAAAT, R: AAGGTAGCGGATGATTCAGCC)
B2M (F: CCAGCAGAGAATGGAAAGTCAA, R: TCTCTCTCCATTCTTCAGTAAGTCAACT)

2.21. mitochondrial DNA/nuclear DNA (mtDNA/nDNA) ratio assay

The copy ratio of mtDNA/nDNA was estimated using extracted genomic DNA using PureLink Genomic DNA Mini Kit (Invitorgen, USA) according to manufacturer's instructions. Then, qPCR was conducted using genomic DNA. The copy number of CYTB was empleyed as mtDNA while B2M as nDNA[41]. Expression levels of CYTB was normalized to B2M using ΔΔCt method and ratio of CYTB/B2M was calculated. The sequences of the primers used in the qPCR are shown below.

2.22. Immunocytochemistry (ICC) assay

ICC assay was performed to visualize cellular mitochondria using MitoTracker Deep Red FM (Invitrogen, USA). Cells were seeded to Lab-Tek II Chamber Slide (NUNC, USA) and stained with 250 nM MitoTracker Deep Red FM at 5% CO2 incubator for 45min. Then, 4% formaldehyde was used to fix the cells at 37 °C for 15 min, 0.5% Triton-X100 was employed for permeabilization for 10 min, and Hoechst 33342 was utilized for nuclear staining for 5 min. Microscope cover glass were mounted using Faramount Mounting Medium, Aqueous (Agilent, USA). Image was visualized using Confocal microscope LSM 700 (Carl Zeiss, Germany).

2.23. XF analysis

The oxygen consumption rate (OCR) was estimated using Seahorse XF HS Mini analyzer (Agilent, USA) with Seahorse XFp Cell Mito Stress Test Kit (Agilent, USA). Cells were seeded into Seahorse XFp Cell Culture Miniplates (Agilent, USA). Subsequently, the media in which the cell lines were incubated was replaced with XF DMEM media (Agilent, USA) supplemented with 4.5 g/L glucose (Agilent, USA), 1 mM pyruvate (Agilent, USA), and 200 mM glutamine (Agilent, USA). OCR value was assessed via serial injection of 2 μM Oligomycin, 2 μM Carbonyl cyanide-p-trifluoromethoxyphenylhydrazone (FCCP), and 1 μM Rotenone/Antimycin A. OCR value was normalized to protein concentration.

3. RESULTS

3.1. TCGA analysis presenting phenotypic differences based on USP14 and UCHL5 in PDAC

First, PAAD from TCGA database was employed to analyze the connotation of USP14 and UCHL5 expression in clinical PDAC patients. The merged transcriptomic data of PAAD and GTEx, normal pancreas tissue database, was used to compare expression levels of USP14 and UCHL5 between normal patient tissues (n = 171) and PDAC patient tissues (n = 179). As expected, given that proteasome activity is high in cancer[20], it showed that PDAC patients exhibited significantly elevated ($p < 0.0001$) expression levels of both genes compare to normal patients (Fig. 1A). Then, Pearson corrlation analysis was conducted to confirm co-expression of both genes. The analysis results presented that expression levels of USP14 and UCHL5 revealed positive correlation coefficient (r = 0.7 and p = 0.0) in PAAD (Fig. 1B). Given that USP14 and UCHL5 localize in a 19S regulatory particle, it might be inferred that the role of both genes could be crucial in PDAC.

Subsequently, PAAD patients were divided into USP14 ^{Low} and USP14 ^{High} groups and UCHL5 ^{High} and UCHL5 ^{Low} based on upper or lower 50% of expression levels. Among the PAAD patients, both USP14 ^{Low} and UCHL ^{Low} patients were designated as USP14/UCHL5 ^{Low} (n = 56), both USP14 ^{High} and UCHL5 ^{High} were designated as USP14/UCHL5 ^{High} (n = 56), and remained patients were designated as Others (n = 66) (Fig. 1C). To investigate distribution of expression patterns, PCA was conducted on the three groups. The result presented that USP14/UCHL5 ^{Low} group was placed at the bottom left position, while USP14/UCHL5 ^{High} group was placed at the top right position (Fig. 1D). Then, Kaplan-Meier analysis was conducted to confirm the survival probability of PAAD. Importantly, USP14/UCHL5 ^{High} patients had a significanctly higher death probability (p = 0.0140) compared to USP14/UCHL5 ^{Low} patients (Fig. 1E). Additionaly, Kapan-Meier plotter database was employed to validate the consistency. The PDAC patients of Kapan-Meier plotter database were divided into top 33% or bottom 33% of USP14 and UCHL5. It showed that patients with high USP14 (p = 0.0022) and UCHL5 (p = 0.0003) expression exhibited a lower survival probability (Fig. 1F-G). It demonstrated that the expression patterns were divided by expression levels of two genes, indicating a kind of phenotypic difference related to survival probability.

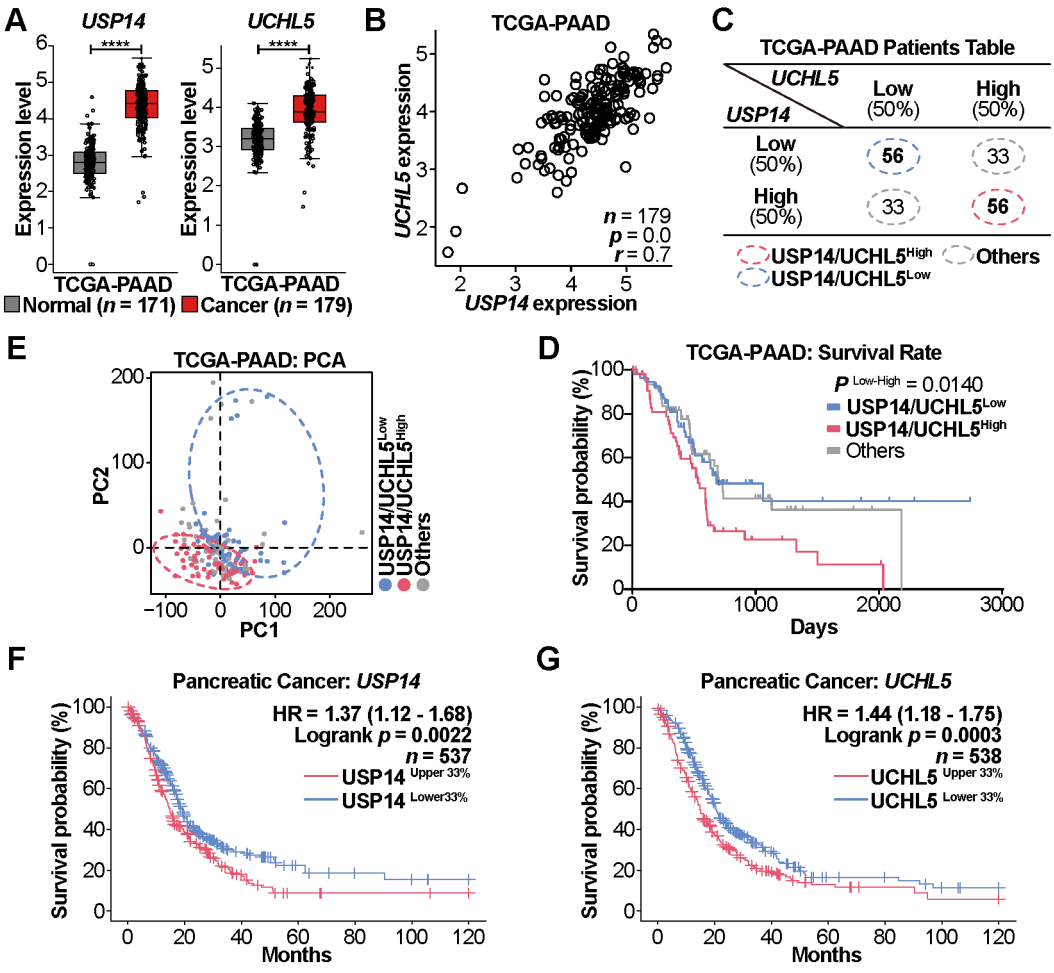

Figure 1. PDAC patients exhibiting different phenotype based on USP14 and UCHL5. (A) Box plot comparing USP14 and UCHL5 expression levels between normal pancreas tissues and PDAC tissues from merged data of PAAD and GTEx. (B) Pearson correlation plot showing the positive correlation (r = 0.7) between USP14 and UCHL5 expression levels in PDAC. (C) Table summarizing the division of PAAD patients based on USP14 and UCHL5 expression levels. (D) PCA plot illustrating phenotypic diffrences between USP14/UCHL5 ^{Low} and USP14/UCHL5 ^{High} groups. (E) Kaplan-Meier curve comparing survivla rate between USP14/UCHL5 ^{Low} and USP14/UCHL5 ^{High} groups. (F-G) Survivlal probability of PDAC patients with top 33% versus botom 33% USP14 and UCHL5 expression levels. **** $p < 0.0001$.

3.2. Spatial expression of USP14 and UCHL5 in PDAC

To investigate spatial RNA expression levels of USP14 and UCHL5, spatial scRNA-seq analysis was conducted. The spatial scRNA-seq data of GSE211895 was collected from GEO database. The samples from three PDAC donors, Patient A, Patient B and Patient C, were analyzed using Seurat package in R. First, the hematoxylin and eosin (H&E) stain and the divided clusters by processing through PCA and UMAP were visualized (Fig. 2A). Each divided cluster was presentative of a unique cell type, the epithelial ductal cells were focused to select malignant cells in PDAC. Marker genes of epithelial ductal cells, *EPCAM* and *TSPAN3,* were utilized. The clusters expressed both *EPCAM* and *TSPAN3* were identified as the epithelial ductal cells, while those that co-expressed the cell proliferation marker genes, *MKI67* and *TOP2A*, were classified as the Cycling Ductal Cell (Patient A: Cluster 2; Patient B: Cluster 0; Patient C: Cluster 2) (Fig. 2B, 2C). Interestingly, the Cycling Ductal Cell cluster was co-localized with the expression levels of USP14 (red) and UCHL5 (blue) along as EPCAM (green) (Fig. 2D). Especially, merged USP14 and UCHL5 (pink) exhibited same expression pattern. The violin plot of USP14 and UCHL5 showed the Cycling Ductal Cell cluster exhibited significantly increased USP14 ($p < 0.0001$) and UCHL5 ($p < 0.0001$) than other clusters (Fig. 2E). The spatial scRNA-seq analysis presented that the expression of USP14 and UCHL5 was highly enriched in the Cycling Ductal Cell clusters, malignant PDAC cells.

Then, to validate the spatial scRNA-seq, IHC was performed using specific antibodies against USP14 and UCHL5. The IHC staining images displayed protein expression levels and were scored as negative (0), weakly positive (1+), moderately positive (2+) and strongly postivie (3+). The score of USP14 was presented as 2+ in normal tissues and 3+ in PDAC (Fig. 3A), while the score of UCHL5 was presented as 0 in normal tissues and 1+ in PDAC (Fig. 3B). The intensity of both genes in epithelial ductal cells showed quantitative value of protein expressions (Fig. 3C). IHC assay presented increased expression levels of USP14 and UCHL5 in PDAC tissues compared to normal. The spatial expression of RNA and protein analysis suggested that both genes were upregulated in ductal cells and they might be therapeutic targets for PDAC patients.

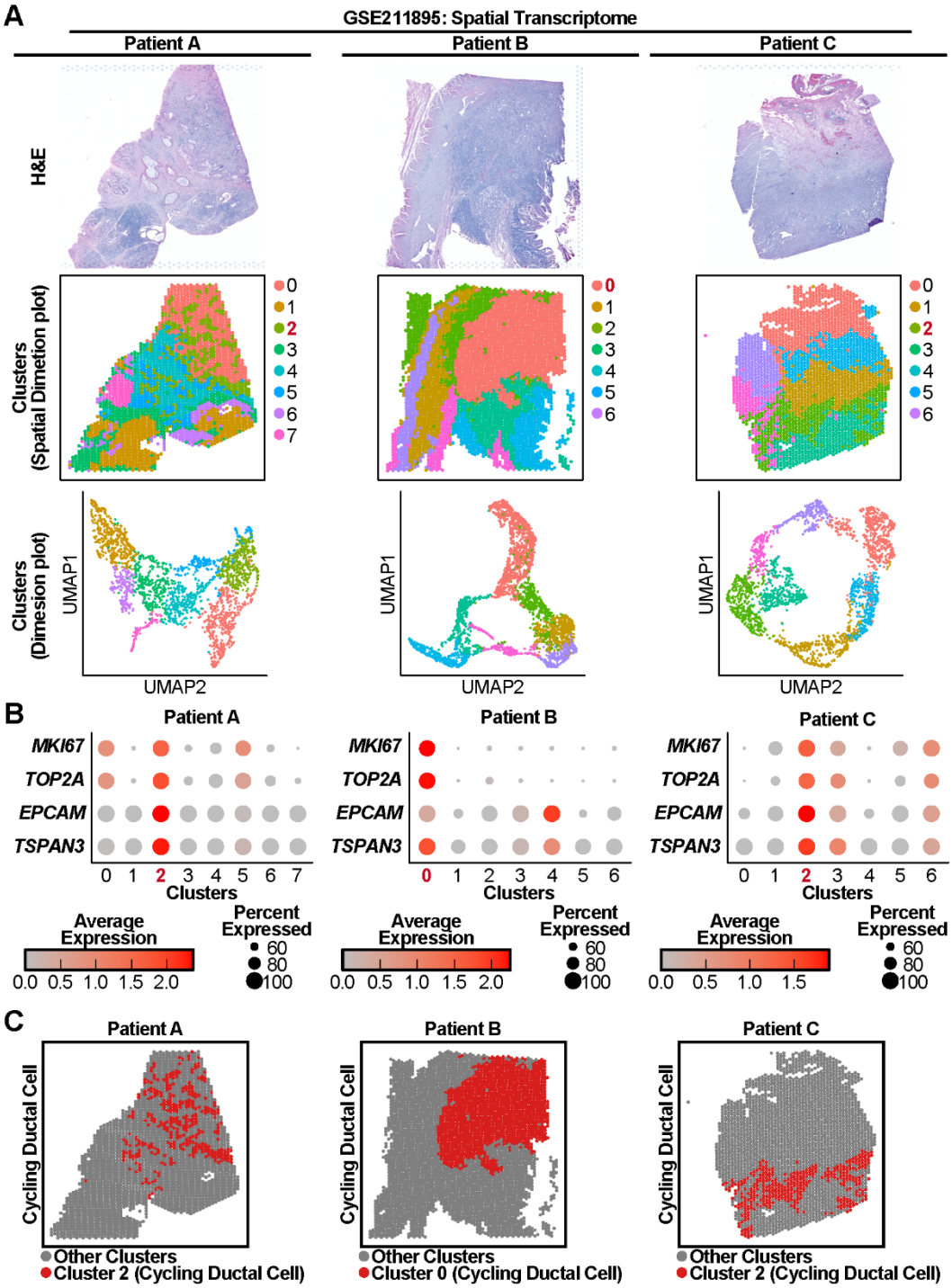

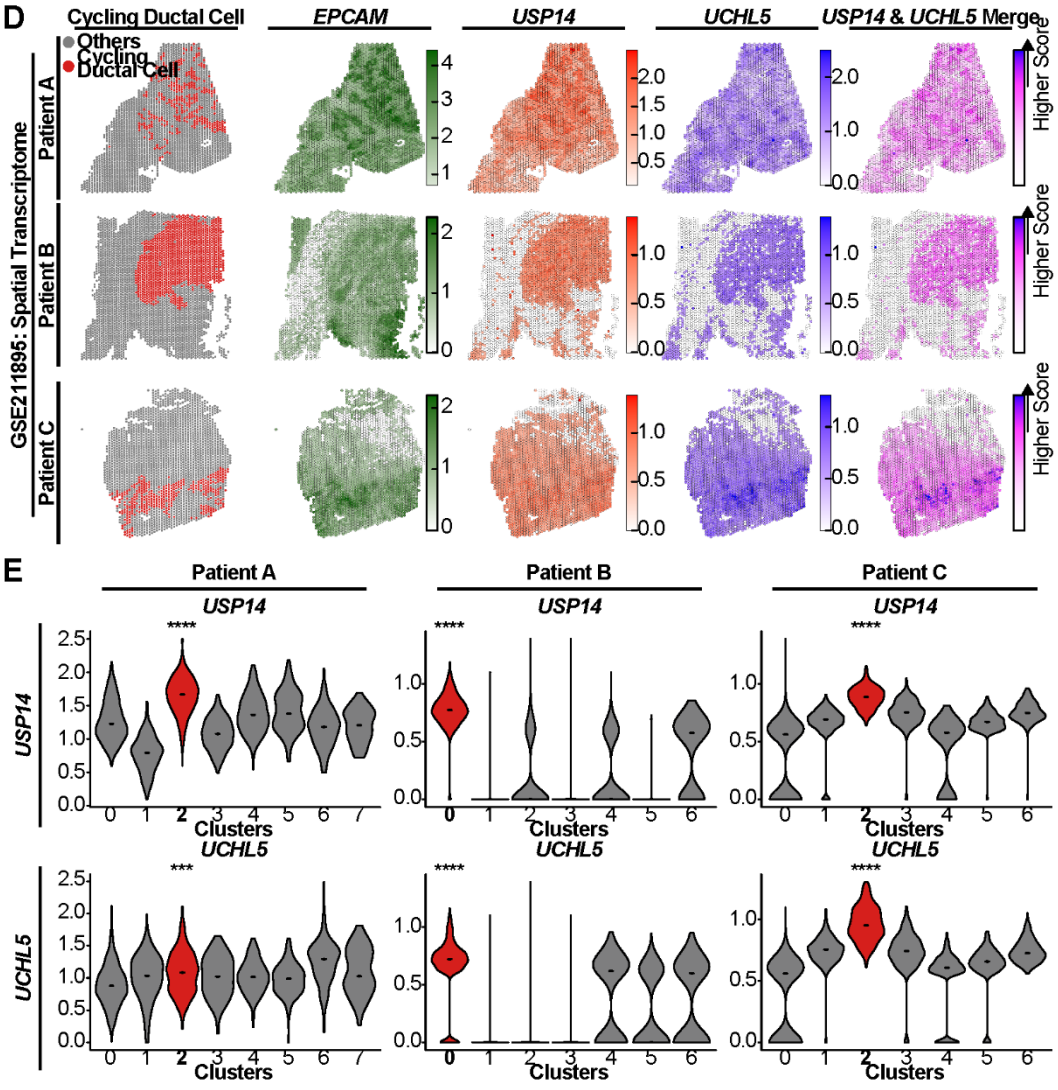

Figure 2. Spatial RNA-seq analysis presenting increased USP14 and UCHL5 in PDAC. (A) Visualizaion of H&E staining of slide, differentiated spatial clusters in slide image and spatial clusters in UMAP. The analysis of spatial scRNA-seq was utilized GSE211895, employed three donors. (B) Dot plots illustrating expression levels of epithelial ductal cell and proliferative cell marker genes across clusters. (C) Dimension plots of the Cycling Ductal Cell clusters. (D) Feature plots of expression of EPCAM (green), USP14 (red), UCHL5 (blue) and merged USP14 and UCHL5

(pink). (E) Violin plots comparing USP14 and UCHL5 expression levels across Cycling Ductal Cell clusters, demonstrating increased expression. * $p < 0.05$, ** $p < 0.01$, *** $p < 0.001$, **** $p < 0.0001$.

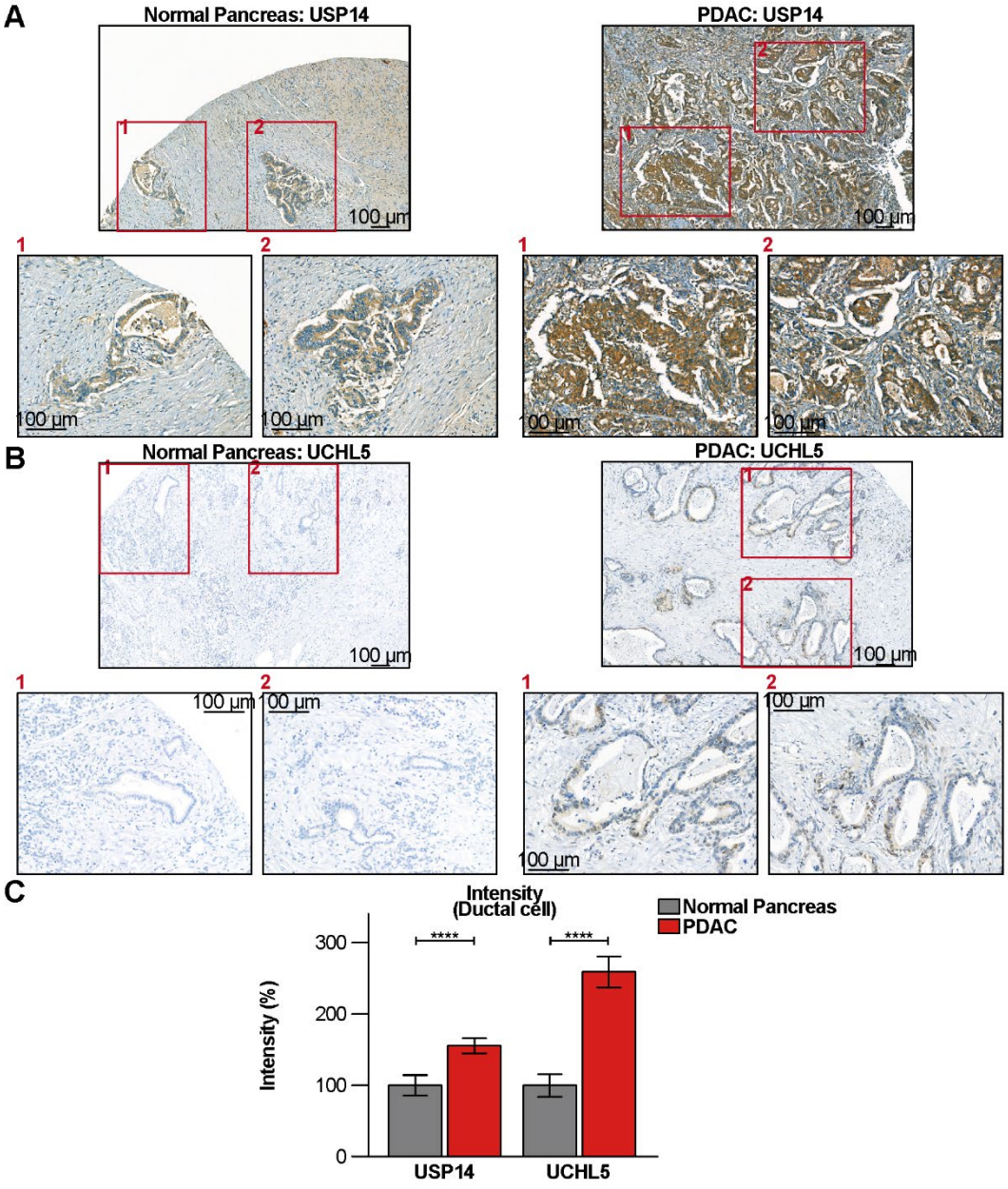

Figure 3. IHC assay presenting increased USP14 and UCHL5 in PDAC. (A) IHC staining for USP14 in normal pancreas (score: 2+) and PDAC (score: 3+) tissues. (B) IHC staining for UCHL5 in normal pancreas (score: 0) and PDAC (score 1+) tissues. (C) Comparison of USP14 and UCHL5 expression intensity in epithelial ductal cells between normal and PDAC tissues. **** $p < 0.0001$.

3.3. Aggressive ductal cells with enhanced USP14 and UCHL5 expression along with proliferation and OXPHOS in PDAC

To overcome the limitation of spatial scRNA-seq, which provides only a bulk resolution per spot, scRNA-seq analysis was performed using the seurat package in R. This method allowed for the identification of various cellular types and facilitated the discovery of additional implications of USP14 and UCHL5 in pancreatic ductal cells. The scRNA-seq data of GSE154778, GSE155698 and GSE212966 were collected from GEO database (Fig. 4A). Total 29 patient samples were downloaded and processed through quality control. Then, integration of the samples was performed to create a merged seurat object. About 100,000 cells were used in scRNA-seq analysis. The cells were performed PCA to reduce demension and the cells were visualized using UMAP, displaying identified 8 different clusters (Fig. 4B). Therefore, distinguished clusters were annotated using marker genes of lineages. Marker genes used for cell differentiation included *CPA3*, *TPSAB1*, *TPSB2* for mast cells, *LUM*, *COL1A1*, *COL5A2* for fibroblasts, *CDH5*, *CLDN5*, *PEACAM1* for endothelial cells, *CD14*, *CD163*, *CD68* for macrophages, *CD19*, *MS4A1*, *CD79A* for B cells, *CD3E*, *CD3D*, *CD8A* for T cells, *CTRC*, *CTRB1*, *PRSS1* for acinar cells and *KRT19*, *TSPAN3*, *SOX9* for ductal cells (Fig. 4C, 4D). The ductal cell cluster was further subsetted to investigate the roles of USP14 and UCHL5 specifically in these cells.

Subsequently, the pseudotime analysis was conducted to research cellular trajectory of differentiation in ductal cells using Monocle3 package and Slingshot package in R. Two pseudotime values were independently calculated and visualized using UMAP (Fig. 5A, 5B). The trajectories indicated by both pseudotime values assessed that the final trajectory was top left side. The correlation between two pseudotime values was evaluated using Pearson correlation analysis (r = 0.84, $p < 0.001$) (Fig. 5C). In order to validate the results of the pseudotime analysis, the cellular proliferation marker genes, *MKI67* and *TOP2A*, were employed. Interestingly, high expression levels of MKI67 and TOP2A were observed at the terminal ends of the pseudotime trajectories, corresponding to highly proliferative cells (Fig. 5D, 5E). Therefore, Subcluster of top left part was designated as Cycling Ductal cell cluster, while remaining cluster was designated as Ductal cell (Fig. 5F). Critically, the Cycling Ductal cell cluster exhibited significantly elevated expression levels of USP14 and UCHL5 (Fig, 5G). Moreover, the positive correlation of USP14 and UCHL5 was demonstrated using Pearson correlation analysis (r = 0.40, $p < 0.0001$) (Fig. 5H). These findings suggest that proliferative ductal cells show increased expression of USP14 and UCHL5, raising the

possibility that these proteins may play a role in malignancy.

GSEA was performed to identify phenotype differences between the Ductal and Cycling Ductal cell clusters. As expected, Cycling Ductal cell cluster displayed increased E2F Targets, MYC targets, G2M Checkpoint and OXPHOS, which are well-known hallmarks of cancer (Fig. 5I). In this study, we focused on E2F targets ($p = 0.0025$), which directly influence cellular growth, and OXPHOS ($p = 0.0026$), which drives energy production (Fig. 5J, 5K). Of particular interest was the finding that cell cycle and mitochondrial function exhibited a positive correlation with USP14 and UCHL5 (Fig. 5L).

Molecular profiling of PDAC tumors divides pancreatic ductal cells into two climical subtypes, classical and basal-like subtypes[42-44]. The classical PDAC subtype exhibits a greater degree of differentiation with more favorable outcomes of patients, while the basal-like PDAC subtype presents less differentiation with worse outcomes of patients. Give that scRNA-seq analysis data were combined with 29 PDAC patients, Cycling Ductal cell clusters could be mixed with two subtypes of tumor ductal cells. Therefore the clusters were divided into Cycling Classical Ductal cells and Cycling Basal-like Ductal cell cluseters based on the expression levels of their marker genes (Fig. 6A). Marker genes used for PDAC subtypes included *GATA3*, *PDX1*, and *HNF4A* for classical ductal cells, *ZEB1*, *FOXM1*, and *VIM* for basal-like ductal cells.

As expected, Cycling Classical Ductal cell and Cycling Basal-like Ductal cell clusters exhibited with higher expression levels of USP14 and UCHL5 than Ductal Cell cluster (Fig. 6B). Interestingly Cycling Basal-like Ductal Cell cluster presented higher expression levels of USP14 than Cycling Classical Ductal cell cluster, while similar expression levels of UCHL5. USP14 seems to be more reflective of the aggressiveness of different subtypes of PDAC than UCHL5. These findings strongly suggest that the proliferative ductal cells are associated with aggressiveness correlated with USP14 and UCHL5 expression.

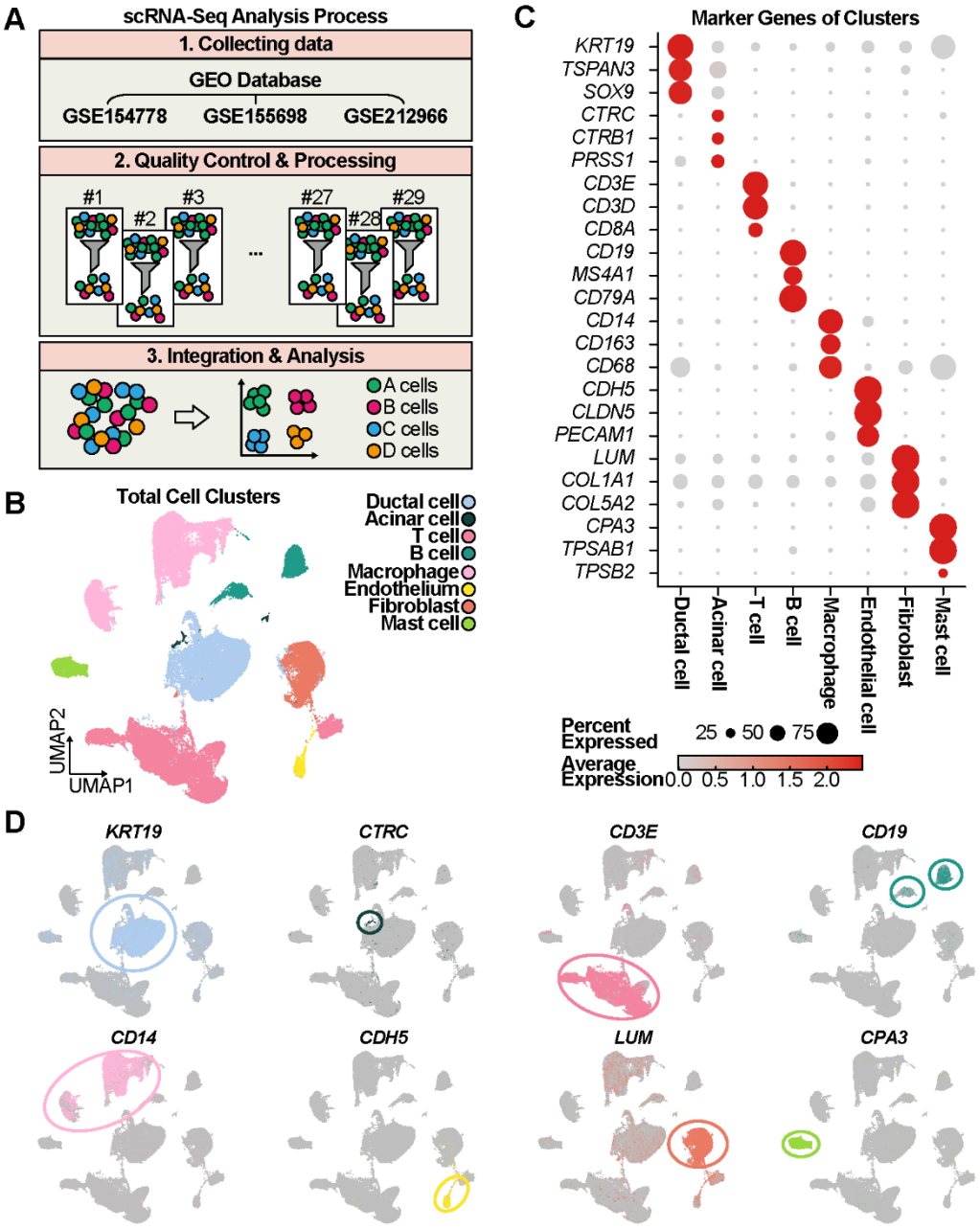

Figure 4. Integration of scRNA-seq data using the 29 PDAC patients. (A) Schematic overview of sample collection and integration process for scRNA-seq analysis. The data from the total 29 PDAC patients were obtained from GSE154778, GSE155698 and GSE212966. (B) Dimension plot illustrating the distribution of 8 PDAC clusters. (C-D) Dot plot and dimension plots presenting the marker genes for the 8 distinc cell clusters.

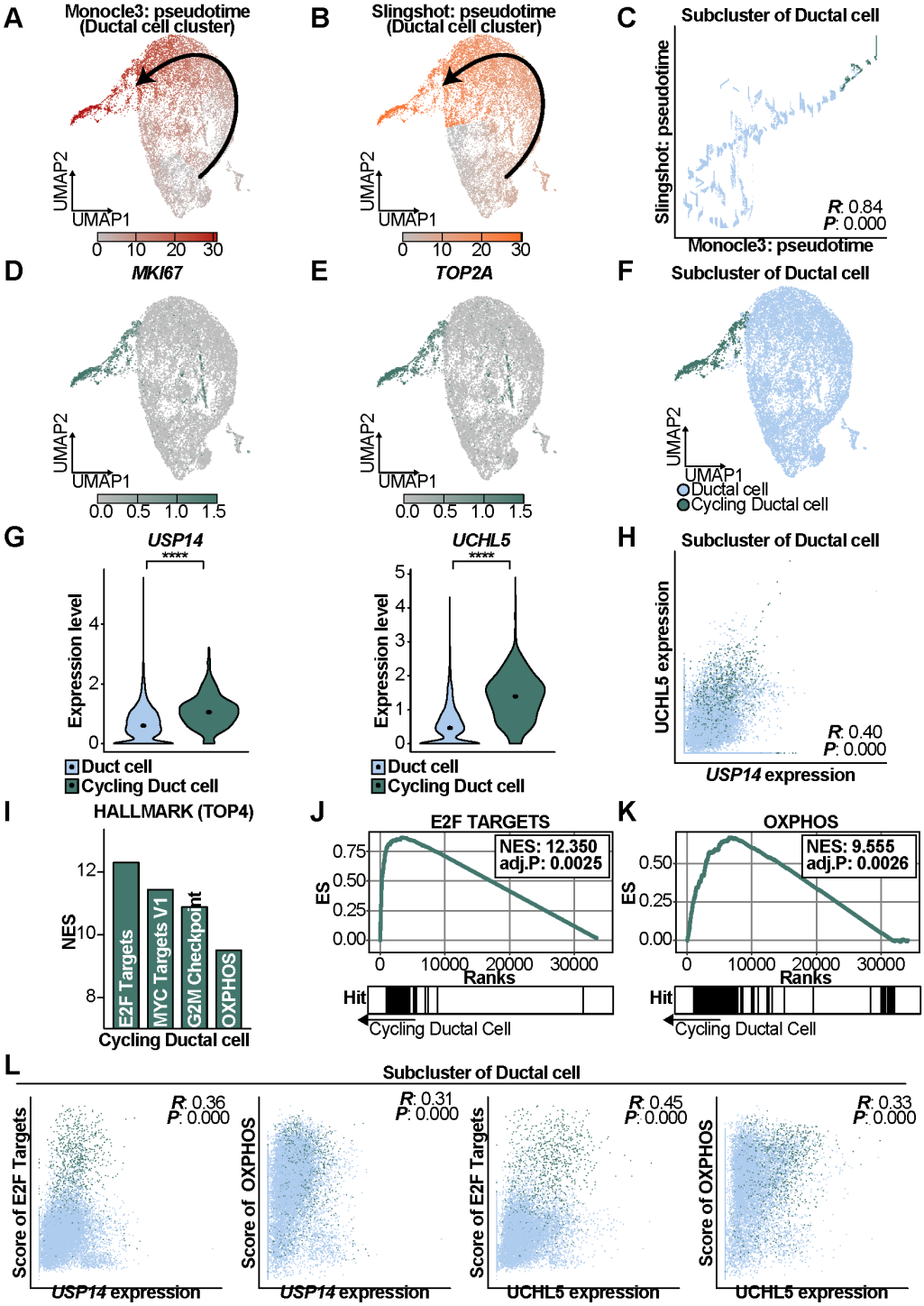

Figure 5. scRNA-seq analysis revealed increased USP14 and UCHL5 concomitant with proliferation and OXPHOS in aggressive ductal cells in PDAC. (A-B) Feature plots of the pseudotime values, the cellullar differentiation trajectory, in ductal cells. The pseudotime values was calculated by Monocle3 and Slingshot package in R. The endpoint of the trajectory is indicated by the top left corner. (C) Correlation plot of two pseudotime values demonstrating positive correlation (r = 0.84) between two pseudotime values in ductal cells. (D-E) Feature plots of *MKI67* and *TOP2A* expression in the ductal cells. (F) Dimension plot of the ductal cells subdivided into Ductal and Cycling Ductal cell group. (G) Violin plot comparing USP14 and UCHL5 expression between the two groups. (H) Correlation plot showing postitive correlation (r = 0.40) between USP14 and UCHL5 expression in the ductal cells. (I) GSEA analysis identified enriched pathways including E2F Targets, MYC Targets, G2M Checkpoints, and OXPHOS in Cycling Ductal cells using the HALLMARK database. (J-K) GSEA enrichment plots for E2F Targets and OXPHOS in the Cycling Ductal cells. (L) Correlation plot presenting the positivie correlation between GSEA results and USP14 or UCHL5 expression in the ductal cells. * $p < 0.05$, ** $p < 0.01$, *** $p < 0.001$, **** $p < 0.0001$.

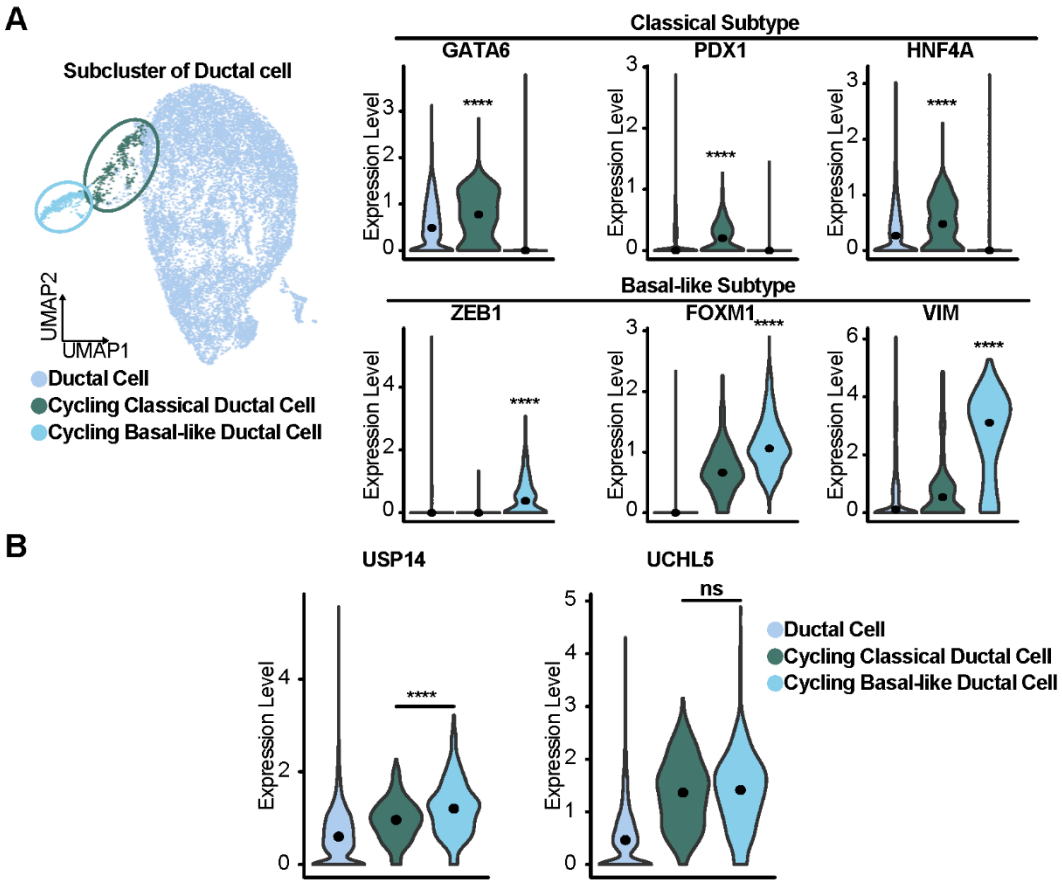

Figure 6. Expression levels of USP14 and UCHL5 in PDAC subtypes. (A) Dimension plot of PDAC subtypes, Ductal Cell, Cycling Classical Ductal Cell and Cycling Basal-like Ductal Cell, with corresponding violin plots depicting the expression of their specific marker genes. (B) Violin plots comparing the expression levels of USP14 and UCHL5 across Ductal Cells, Cycling Classical Ductal Cells, and Cycling Basal-like Ductal Cells. * $p < 0.05$, ** $p < 0.01$, *** $p < 0.001$, **** $p < 0.0001$.

3.4. Dual inhibition of USP14 and UCHL5 by b-AP15 suppressed proliferation of PDAC

The clinical implications of USP14 and UCHL5 in PDAC was elucidated that aggressive ductal cells exhibited upregulated expression of both genes by the previous clinical analysis. Importantly, the ductal cells with higher expression of USP14 and UCHL5 enhanced proliferation and OXPHOS activity, which could influence the patient's survival probability. These findings lead to the hypothesis that USP14 and UCHL5 play a critical role in PDAC and possibility for therapeutic targets. To explore the potential of USP14 and UCHL5 as therapeutic targets, the PDAC cell lines, PANC1 and MIAPACA2 were employed[45]. Both cell lines have been used as in vitro models for PDAC for decades. USP14 and UCHL5 were inhibited using b-AP15[33], specific dual inhibitor.

The proliferation rates of PANC1 and MIAPACA2 were determined to determine the efficacy of inhibiting PDAC cell growth. The PDAC cells were incubated with vehicle control, 1 μM and 2 μM b-AP15 and measured proliferation rate at 0, 24, 48 and 72 hr time point. The assay results revealed that inhibition of cell multiplication was confirmed at 1 μM b-AP15 ($p < 0.0001$) and 2 μM b-AP15 ($p < 0.0001$) (Fig. 7A). The process of cell division was observed to be virtually halted, confirmed by colony formation assay. The central region of the cell plate of 1 μM b-AP15 formed fewer colonies compared to the control group (Fig. 7B). The slowed cell proliferation was also demonstrated in a wound healing assay. The wound area of scratched cells showed that the b-AP15 group was significantly higher than the control group (PANC1 $p = 0.0016$, MIAPACA2 $p = 0.0035$) (Fig. 7C). To determine the cell cycle phase of the slowed proliferation, it was measured by flowcytometry using propidium iodide. The analysis results revealed that cell growth inhibition using 1 μM b-AP15 resulted in significant accumulation of cells in the G1 phase (PANC1 $p < 0.0001$, MIAPACA2 $p < 0.0001$) compared to control group (Fig. 7D). These findings suggested inhibition of USP14 and UCHL5 could reduce cell proliferation in PDAC cell lines.

The xenograft models were developed to assess the ability of b-AP15 to inhibit PDAC proliferation in vivo. The BALB/c nude mice, an immunodeficient models, were implanted with MIAPACA2 cells, which exhibit benefit with a faster growth rate than PANC1 cells. Mixtures of suspended MIAPACA2 cells with Matrigel were injected to right plank of mices and implanted mices were randomly splited into control group ($n = 8$) and b-AP15 group ($n = 8$). Day 0 was defined as the time when the tumor volume about 100 mm^3 per group (control group $v = 96.1$ mm^3, b-AP15 group $v = 99.1$ mm^3, $p = 0.852$) (Fig 8A). From that Day 0 on, 7.5 mg/kg b-AP15 was injected

intraperitoneally three times a week until the tumor volume reached 2,000 mm^3. Mice were sacrificed on Day 27 when the largest tumor volume in the control group measured 1890 mm^3. Tumor volume measured from Day 0 to Day 27 showed that tumor growth was significantly inhibited (Day27 $p = 0.0008$) in the b-AP15 group (Fig. 8B). Tumors were extracted from mice and weighed, and a significant reduction ($p = 0.0024$) in tumor weight was observed, similar to the reduction in volume (Fig. 8C). Lastly, the extracted tumor was visualized (Fig, 8C). The results of both in vitro and in vivo experiments indicated that the inhibition of USP14 and UCHL5 is an effective method for reducing the proliferation of PDAC models.

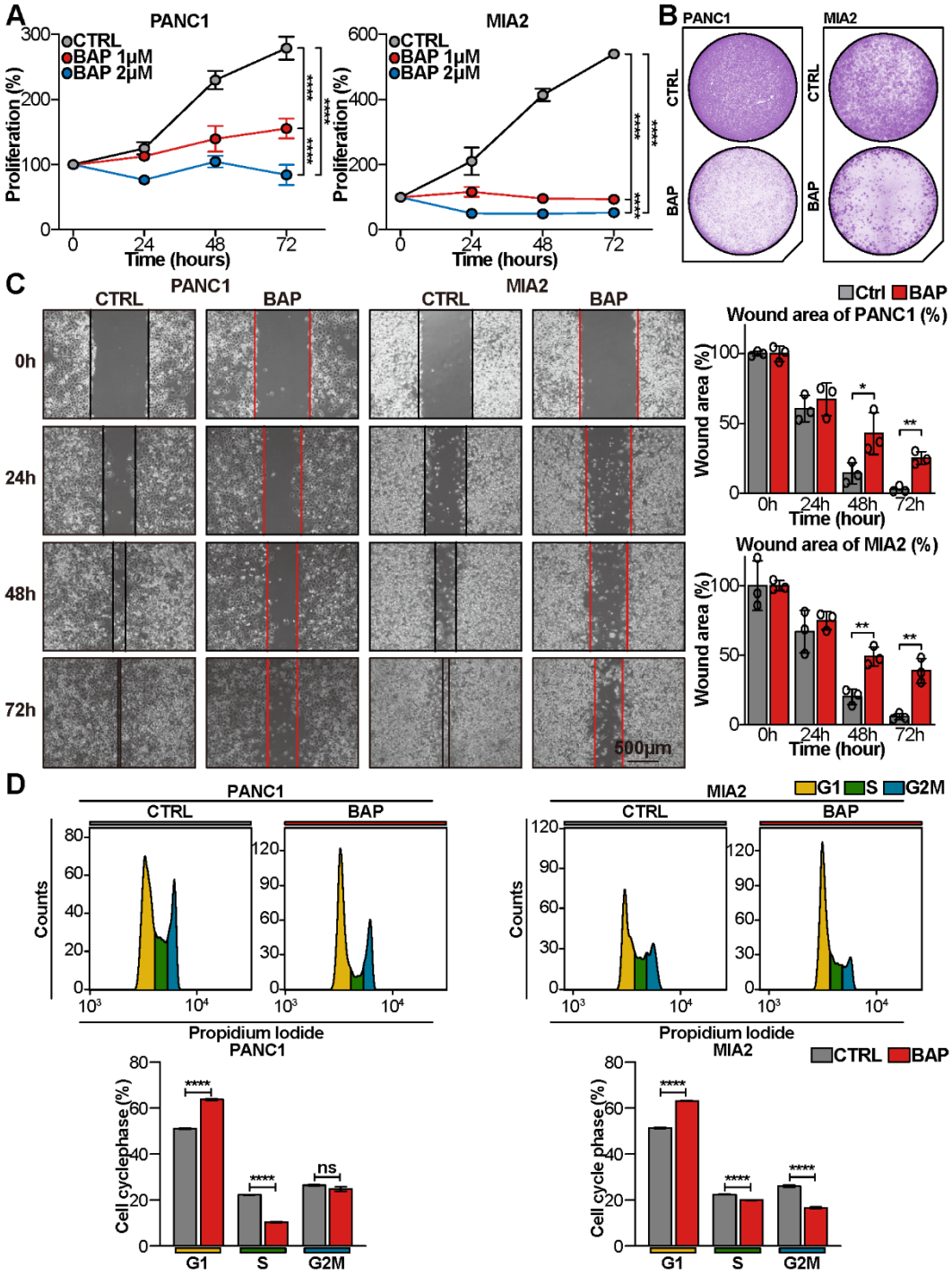

Figure 7. USP14 and UCHL5 inhibition suppressed proliferation of PDAC cell lines. (A) Proliferation curve of PDAC cells treated with vehicle, 1 μM and 2 μM b-AP15. (B) Colony formation assay demonstrating reduced cell growth in the b-AP15 group compared to the control. (C) Wound healing assay showing differences in cell migration speed between control and b-AP15 groups. (D) Cell cycle analysis showing a significant G1 phase arrest in the b-AP15 group compared to the control, as illustrated by histogram and bar plot representations of cell cycle phase distribution. * $p < 0.05$, ** $p < 0.01$, *** $p < 0.001$, **** $p < 0.0001$.

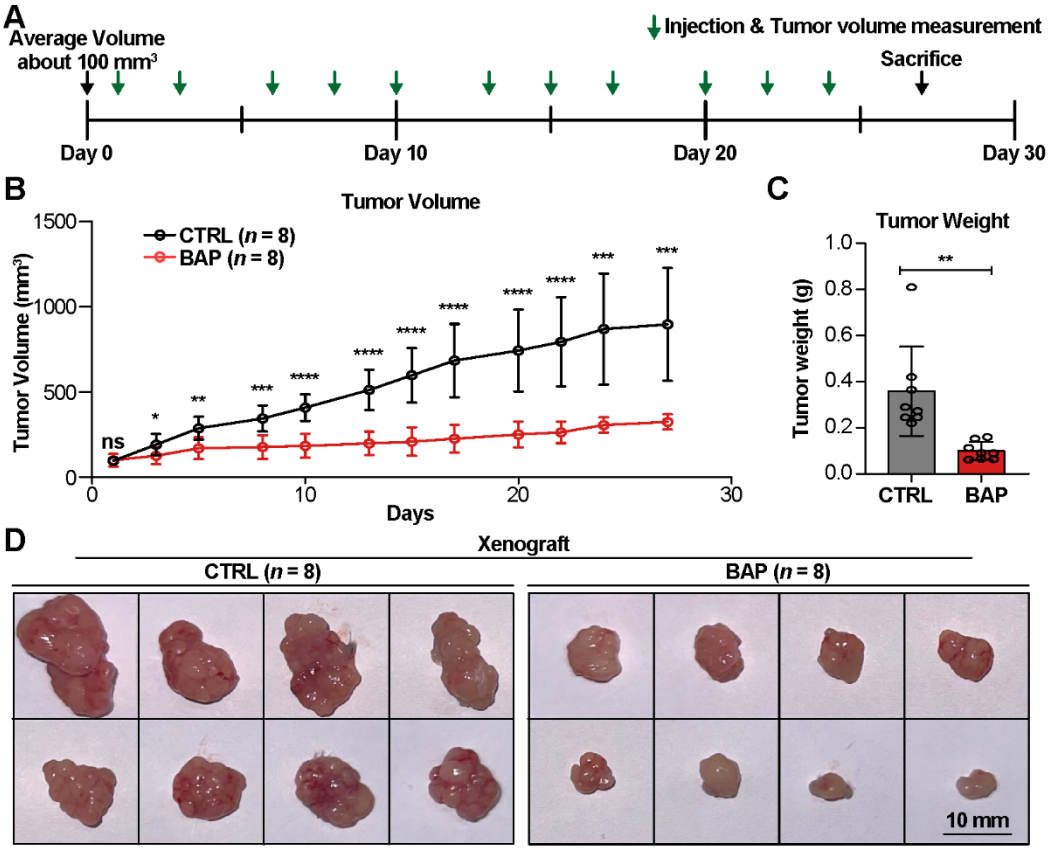

Figure 8. USP14 and UCHL5 inhibition suppressed tumor growth in PDAC xenograft models. (A) Experimental schematic of PDAC xenograft models. Tumor growth was monitored until Day 27, prior to reaching a maximum volume of 2000 mm³. (B) Tumor growth curves demonstrating significantly reduced tumor volume (Day27 $p < 0.0001$) in the b-AP15 group. (C) Bar plot comparing tumor weight between control and b-AP15 groups. (D) Representative images of extracted tumors from xenograft models illustrating suppressed tumor proliferation in the b-AP15 group. * $p < 0.05$, ** $p < 0.01$, *** $p < 0.001$, **** $p < 0.0001$.

3.5. Proteomics and transcriptomics analyses revealed that USP14 and UCHL5 inhibition triggered proteotoxic stress and mitochondrial dysfunction in PDAC

Previous findings demonstrated that USP14 and UCHL5 inhibition using b-AP15 strongly suppressed proliferation of PDAC in vitro and in vivo models. In order to gain insight into the mechanisms by which the inhibition of proteasomal deubiquitinases affects cell growth, investigation at both the protein and RNA levels was conducted.

To assess the expression levels of proteins and RNA, proteomic and transcriptomic analyses were performed by LC/MS and bulk RNA-seq (Fig. 9A). For LC/MS For LC/MS, FASP-digested protein samples were analyzed by mass spectrometry, and protein abundance was quantified using Proteome Discoverer software. For bulk RNA-seq, fragmented RNA samples were ligated with unique adapters at their 5' and 3' ends to generate cDNA fragments suitable for library construction and sequencing. The FASTQ files, generated by the Illumina sequencing platform, were subjected to processing to estimate the expression levels of RNA. The protein and RNA expression levels obtained were employed in the analysis of the mechanisms underlying the effects of b-AP15. In both cases of differentially expressed proteins (DEP; fold change ≥ 2, $p < 0.05$) and differentially expressed genes (DEG; fold change ≥ 2, $p < 0.05$), the number of upregulated proteins/genes exceeded than that of downregulated (Fig. 8A). Nevertheless, there was a paucity of overlapping proteins/genes between DEP and DEG, and thus they were not employed in analysis.

Therefore, instead of utilizing DEP and DEG, we performed GSEA using total proteins/genes with Gene Ontology (GO) database. Enrichment maps were generated by GSEA results with the normalized enrichment score (NES) ($p < 0.05$) in the same direction of between both cells using the EnrichmentMap in Cytoscape (Fig. 9B). Subsequently, the related nodes were grouped by the AutoAnnotate in Cytoscape. The enrichment map demonstrated a reduction of the respiratory complex activity in the protein/gene levels and increased unfolded protein response (UPR) activity. This finding was supported by the top and bottom 10 NES of GO gene sets in the GSEA results using bulk RNA-seq (Fig. 9C). The NES of UPR-related genes, such as those involved in protein refolding and chaperone activity, was observed to increase, while the NES of mitochondrial complex and OXPHOS-related genes was found to decrease. GSEA using the HALLMARK database demonstrated increased UPR (PANC1 $p = 0.028$, MIA2PACA2 $p = 0.033$) and decreased OXPHOS

(PANC1 p = 0.000, MIAPACA2 p = 0.022), exhibiting consistency with the GO database (Fig. 9D).

The top 10 gene sets from the GO database were used to analyze overlapping genes for each set (Fig. 9E). Among the upregulated gene sets, multiple 70-kilodalton heat shock protein (HSP70) family members, including *HSPA6* and *HSPA1A*, were shared by PANC1 and MIAPACA2. Conversely, downregulated respiratory complex genes such as *NDUFA2*, *NDUFA3*, *NDUFA7*, *NDUFC1*, and *NDUFS7* were common to both cell lines. A volcano plot of LC/MS and bulk RNA-seq fold change revealed increased chaperone and ubiquitin proteins/genes and decreased mitochondrial proteins/genes (Fig. 9F). Interestingly, the volcano plot demonstrated the accumulation of ubiquitin, which resulted from the inability of ubiquitinated substrates to undergo degradation due to the inhibition of USP14 and UCHL5. Notably, the reduced expression of mitochondrial respiratory complex genes, essential for efficient energy production through OXPHOS, suggests impaired mitochondrial biosynthesis. Given the established link between mitochondrial gene expression and cellular function of ERRα, I hypothesize that decreased ERRα activity contributed to reduced mitochondrial biosynthesis.

To confirm the activity of ERRα, the motif activity of ERRα, ERRE, was focused on. Identified using JASPAR CORE 2024[46], ERRE has the sequence TCAAGGTCA (Fig. 9G) and is essential for ERRα DNA binding. Integrated Motif Activity Response Analysis (ISMARA) was performed with bulk RNA-seq. ISMARA estimates transcription factor activity based on gene expression changes associated with the presence of their binding motifs. By correlating gene expression with motif enrichment, ISMARA quantifies the impact of transcription factors on gene regulation. The ISMARA results demonstrated that reduced motif activity of ERRα in both b-AP15 treated cell groups (Fig. 9H).

The presented proteomic and transcriptomic data indicated that PDAC cells treated with b-AP exhibited augmented UPR and, conversely, diminished OXPHOS, suggesting impaired mitochondrial function. To elucidate the underlying mechanisms linking USP14 and UCHL5 inhibition to these phenotypic changes, further in vitro mechanistic studies were required.

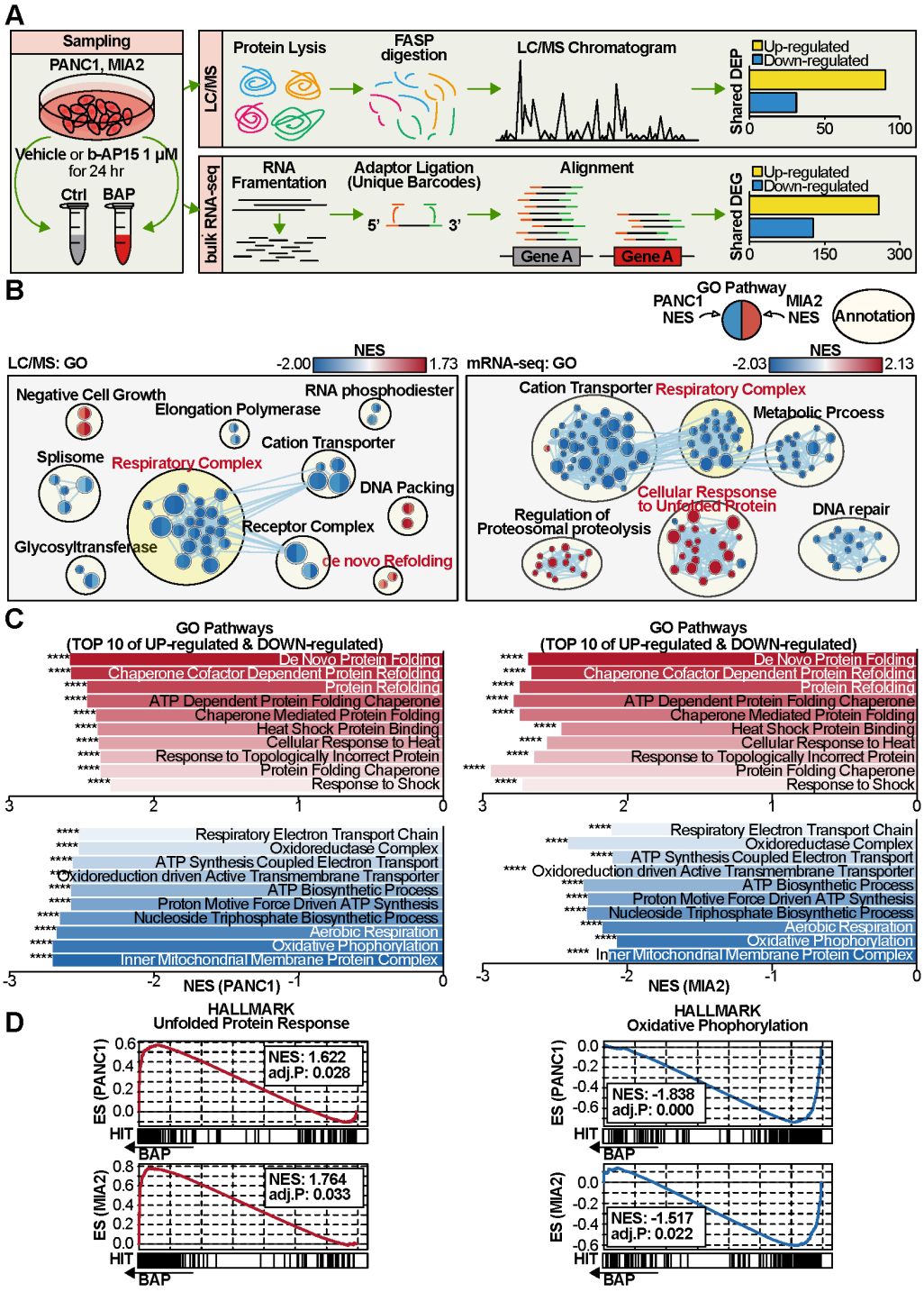

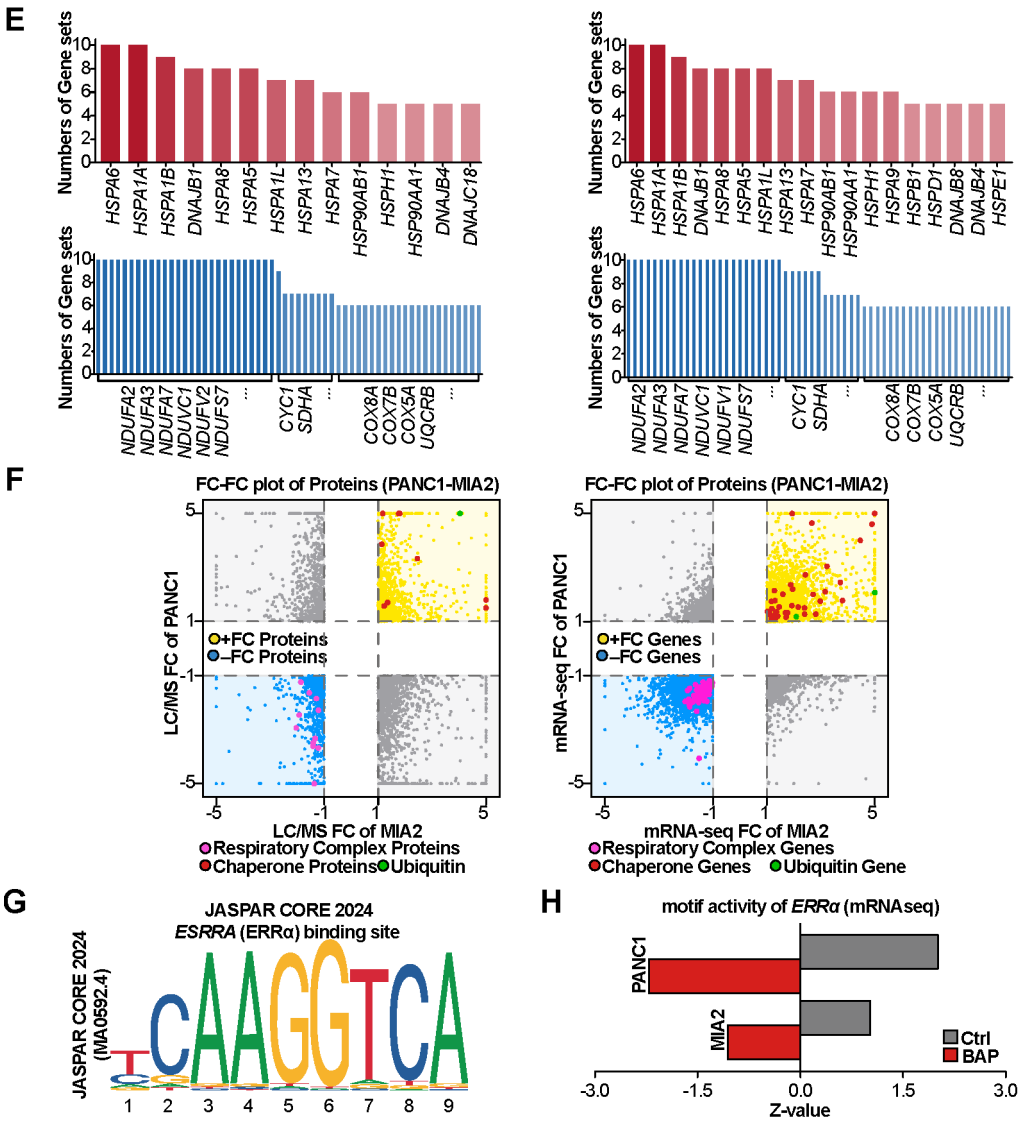

Figure 9. b-AP15 inducing increased UPR activity and decreased OXPHOS activity using LC/MS and **bulk RNA-seq analysis in PDAC.** (A) Experimental schematic of LC/MS and bulk RNA-seq analysis. (B) Enrichment map illustrating positive (red) and negative (blue) NES values of LC/MS and bulk RNA-seq using GO database. (C) Bar plots of positive and negative top 10 NES values of PANC1 and MIAPACA2 using GO database. (D) Enrichment plot showing increased NES of UPR (PANC1 p = 0.028, MIAPACA2 p = 0.033) and decreased NES of OXPHOS (PANC1 p = 0.000,

and MIAPACA2 $p = 0.022$) in both cell lines. (E) Overlapping genes of gene sets using top 10 GO database. (F) Volcano plots of LC/MS and bulk RNA-seq showing decreased fold change of chaperone and ubiquitin proteins/genes, and increased respiratory complex proteins/genes. (G) Sequence logo of ERRE, ERRα binding motif sequence, presenting sequence TCAAGGTCA. (H) Motif activity of ERRα comparing control and b-AP15 in PANC1 and MIAPACA2. * $p < 0.05$, ** $p < 0.01$, *** $p < 0.001$, **** $p < 0.0001$.

3.6. UPR induced by USP14 and UCHL5 inhibition led accumulation of oxidized proteins in PDAC

First, experiments were conducted to identify proteomic and transcriptomic phenotypic changes in PDAC cells treated with b-AP15. In the normal condition of UPS cells, ubiquitinated substrates are deubiquitinated and degraded by proteasomal deubiquitinases (Fig. 10A). Nevertheless, the inhibition of USP14 and UCHL5, which are components of the 19S regulatory particle of the proteasome, resulted in the accumulation of ubiquitin (Fig. 10B). Immunoblot analysis of ubiquitin revealed that the increased accumulation of ubiquitin, particularly high-molecular-weight proteins. Among the ubiquitins, K48-ubiquitin, which is known to be subject to proteasomal degradation, demonstrated the most significant accumulation of ubiquitin in b-AP15 groups. The ubiquitin data confirmed the accumulation of ubiquitinated substrates with USP14 and UCHL5 inhibition as theorized.

The endoplasmic reticulum (ER) is an intracellular organelle that plays a povital role in protein biosynthesis. The ER induces the UPR to address accumulated unfolded and misfolded proteins, kwown as ER stress, before they cause catastrophic damage to the cell[47]. Protein kinase R-like endoplasmic reticulum kinase (PERK/*EIF2AK3*) detects the accumulation of unfolded or misfolded proteins in the ER lumen[48]. Subsequently, the phosphorylation of PERK, which is an activated form of PERK, facilitates the translation of activating transcription factor 4 (ATF4) in response to ER stress[49]. The ubiquitinated substrates accumulation by USP14 and UCHL5 inhibition induced significantly increased RNA expression levels ($p < 0.0001$) of ATF4 (Fig. 9C). The RNA expression levels of DNA damage inducible transcript 3 (*DDIT3*) and *ATF3*, which are downstream target genes of ATF4[50], were increased ($p < 0.0001$) in b-AP15 groups (Fig. 9C). In addition, RNA expression levels of chaperones, *HSPA1*, *HSPA6* and *DNAJA1*, were significantly increased in b-AP15, according to bulk RNA-seq (Fig. 9E, 9F, 10D).

Given, the established relationship between induced ER stress, oxidative stress and redox system[51-54], the study focused on this particular aspect (Fig. 11A). The level of oxidative stress was quantified by measuring the intracellular ROS using the DCFDA assay, which revealed a significant increase in PANC1 ($p < 0.0001$) and MIAPACA2 ($p < 0.0001$) of the b-AP15 groups (Fig. 11B). The expression levels of SOD1, which catalyzes the conversion of superoxide ($O_2^{\bullet-}$) to hydrogen peroxide (H_2O_2)[55], was significantly elevated in b-AP15 group. In addition, the expression levels of

HMOX1, signature of oxidative stress[56,57], was also increased in b-AP15 group. The increased SOD1, ROS and HMOX1 by USP14 and UCHL5 inhibition demonstrated that critical oxidative stress was induced.

In the glutathione in redox system, the tripeptide glutathione (GSH) is converted to glutathione disulfide (GSSG) by the reduction of ROS to H_2O[58,59]. Glutathione synthetase (GSS) synthesizes glutathione, while glutathione peroxidase 1 (GPX1) and GPX4 directly reduce ROS using GSH. Interestingly, the redox system was impaired in b-AP15 group (Fig. 11C). The expression levels of GSS, GPX1 and GPX4 were significantly reduced in b-AP15 group in PDAC cells. Importantly, the GSH/GSSG ratio decreased significantly from 27.2 to 8.7 in PANC1 ($p = 0.0003$) and 26.7 to 7.2 in MIAPACA2 ($p = 0.0010$).

The inhibition of USP14 and UCHL5 suppressed proteasomal degradation and led accumulation of the ubiquitinated substrates. It induced ER stress, oxidative stress, and impaired redox system. The accumulated ROS with disturbed redox system eventually ushered to protein oxidation (Fig. 11D), which would have affected cell proliferation[60,61].

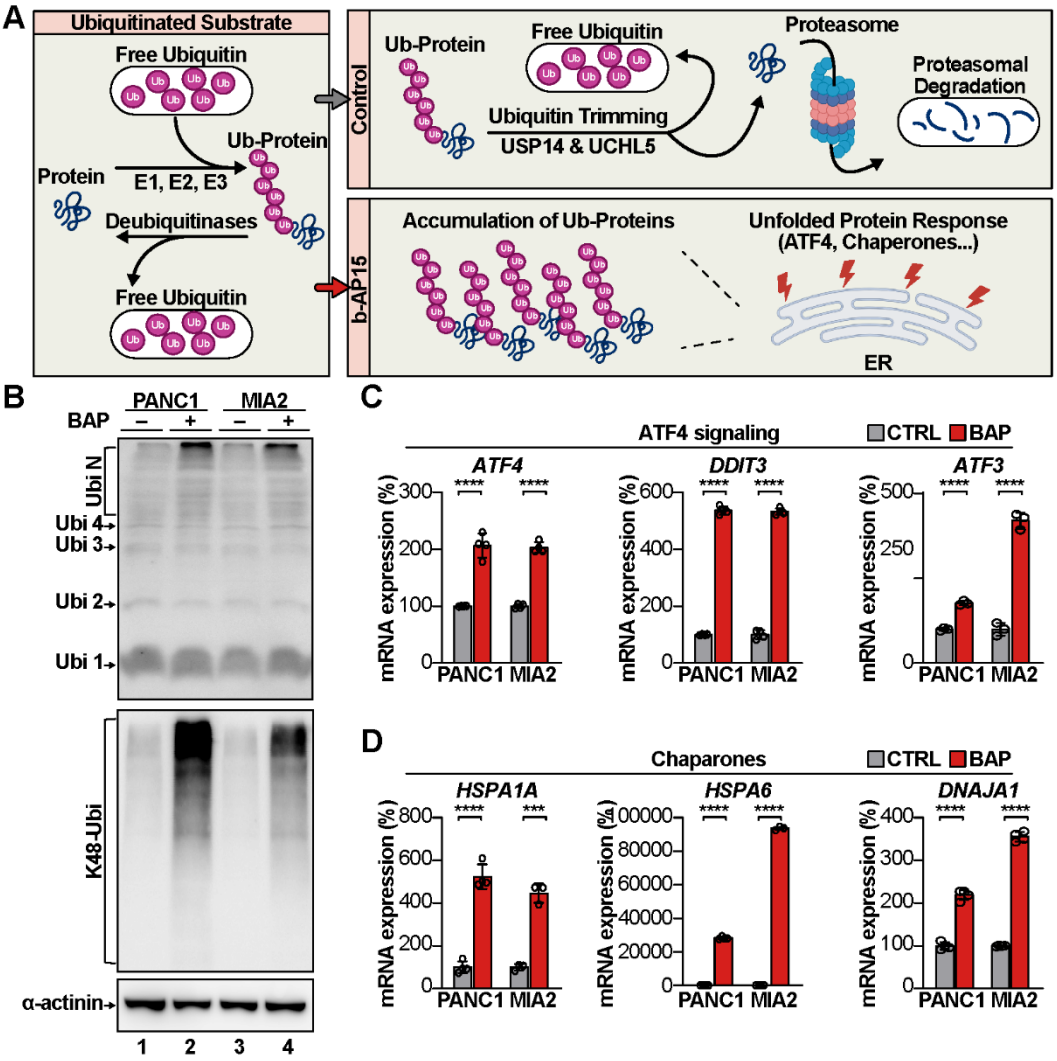

Figure 10. b-AP15 induced UPR in PDAC. (A) Mechanism of UPR induced by b-AP15 in PDAC cells. Accumulatio of ubiquitinated substrates led ATF4 signaling and chaperone genes expressions. (B) Immunoblotting of Ubiquitins and K48-Ubiquitins in PANC1 and MIAPACA2. (C) Bar plots of ATF4 signaling genes presenting increased expression levels of ATF4, DDIT3 and ATF3 in b-AP15 groups. (D) Bar plots of chaperone genes showing increased expression levels of HSPA1A, HSPA6 and DNAJA1 in b-AP15 groups. * $p < 0.05$, ** $p < 0.01$, *** $p < 0.001$, **** $p < 0.0001$.

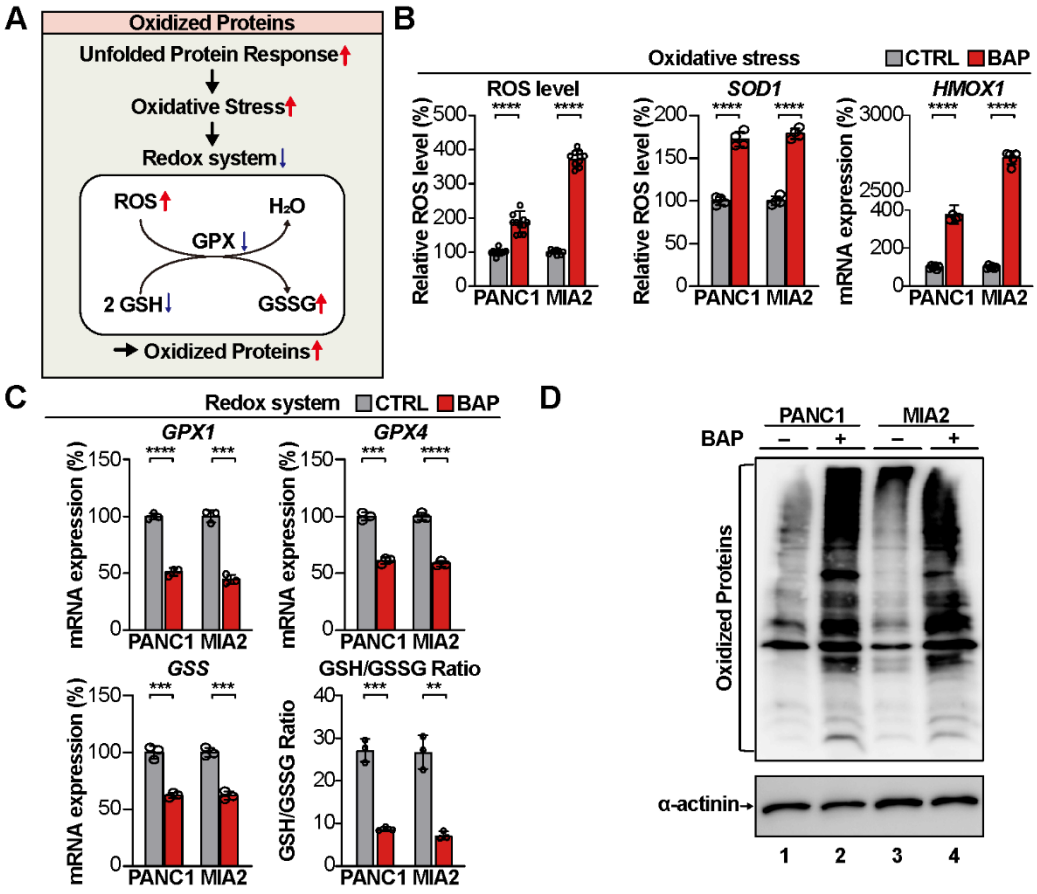

Figure 11. Accumulation of oxidized proteins mediated UPR in PDAC. (A) Schemic process of accumulation of oxidized proteins. (B) Bar plots of ROS, SOD1 and HMOX1 comparing between control and b-AP15 groups. (C) Bar plots of GPX1, GPX4, GSS and GSH/GSSG ratio comparing between control and b-AP15 groups. (D) Accumulation of oxidized proteins in b-AP15 treated PDAC cells. * $p < 0.05$, ** $p < 0.01$, *** $p < 0.001$, **** $p < 0.0001$.

3.7. Autophagic lysosomal degradation of ERRα mediated by the USP14 and UCHL5 inhibition

Inhibition of USP14 and UCHL5 led to the accumulation of oxidized proteins, which, together with increased UPR and oxidative stress, could critically affect cancer cell growth. To investigate how this oxidative stress leads to reduced OXPHOS, the expression levels of ERRα were analyzed at both RNA and protein levels, focusing on transcription and translation. Despite the decreased ERRα motif activity observed in bulk RNA-seq analysis (Fig. 9H), the RNA expression levels of ERRα were not significantly different between the control and b-AP15 groups (Fig. 12A). However, the protein expression levels of ERRα were reduced in the b-AP15 group (Fig. 12B). Treatment with 1 μM b-AP15 resulted in a time-dependent decrease in protein expression levels of ERRα in both cell lines at 0, 3, 6, 12 and 24 h. In addition, treatment with 0.0, 0.5, 1.0 and 2.0 μM b-AP15 at 24 h decreased protein expression levels of ERRα in a dose-dependent manner. This suggests that while ERRα was continuously transcribed at the RNA level, its protein levels were reduced due to enhanced cellular degradation in the b-AP15-treated group.

MG132, a proteasome inhibitor[62,63], and Bafilimycin A1, an autophagy inhibitor[64,65], were used to determine if ERRα degradation occurred via the proteasomal or autophagic-lysosomal pathways. Cells were treated with b-AP15 for 12 h, followed by treatment with 10 μM MG132 for 8 to 10 hours, which did not affect ERRα protein expression levels (Fig. 12C). In contrast, treatment with 400 nM Bafilomycin A1 for 6 to 12 hours reversed the decreased ERRα expression levels in both cell lines (Fig. 12D). These findings demonstrated that autophagy, triggered by the inhibition of USP14 and UCHL5, resulted in the lysosomal degradation of ERRα.

To further investigate the interaction of ERRα-USP14, and ERRα-UCHL5, immunoprecipitation assay was performed using overexpressed 293T cell lysates. ERRα was overexpressed with USP14 or UCHL5 in 293T cells and harvested to determine direct interactions of these proteins. As expected, formation of protein complexes of ERRα-USP14 and ERRα-UCHL5 was confirmed by immunoprecipitation assay (Fig. 13A, 13B). These data suggest that ERRα may serve as a common regulatory target of USP14 and UCHL5, potentially contributing to its proteasomal degradation. Inhibition of USP14 and UCHL5 shifted ERRα degradation from a proteasomal to an autophagic pathway.

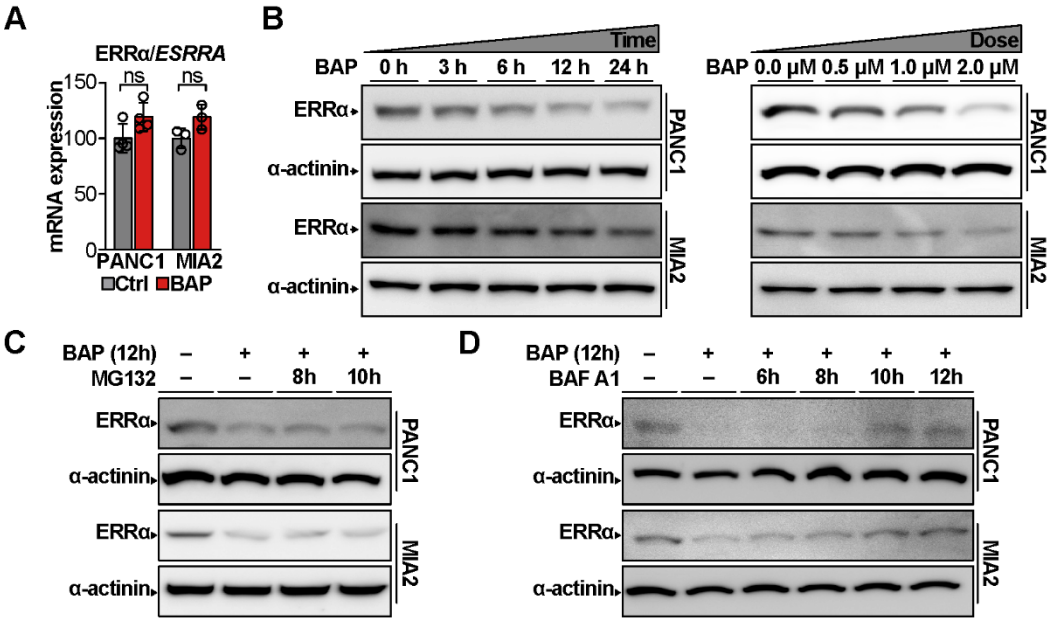

Figure 12. USP14 and UCHL5 inhibition reduced ERRα expression by autophagic lysosomal degradation in PDAC**.** (A) RNA expression levels of ERRα comparing control and b-AP15 groups in PDAC. (B) Immunoblot images illustrating decreased ERRα expression in response to time-dependent and dose-dependent b-AP15 treatment in PDAC cells. (C, D) Immunoblot images of ERRα expression in response to b-AP15 treatment with MG132 or Bafilomycin A1. * $p < 0.05$, ** $p < 0.01$, *** $p < 0.001$, **** $p < 0.0001$.

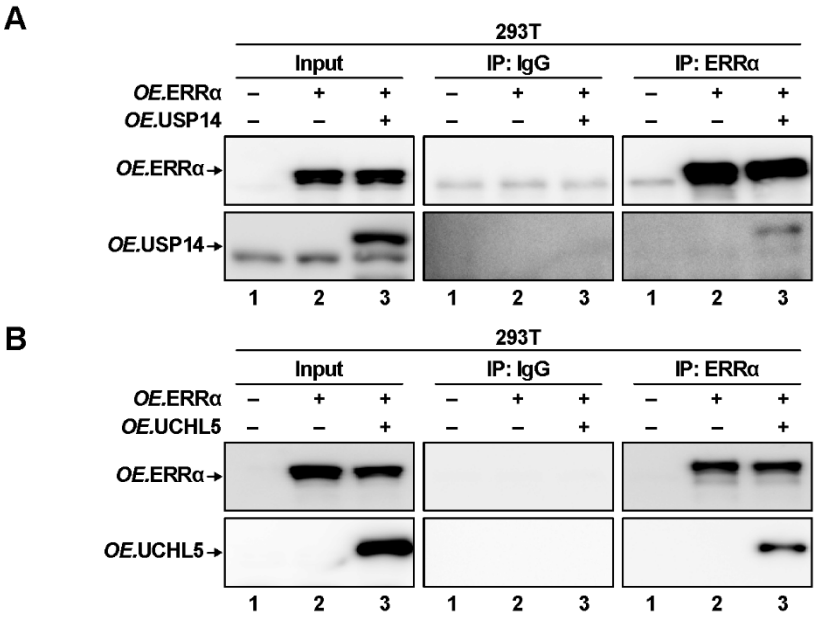

Figure 13. Immunoprecipitation assay presenting protein complexes between ERRα, USP14 and UCHL5. (A, B) Immunoblot images of USP14 and UCHL5 immunoprecipitated by ERRα antibody. Proteiens extracted from cell lysates were obtained from 293T cells overexpressing ERRα along with USP14 or UCHL5. Input samples (left), immunoprecipitation with IgG control (IP: IgG; middle), and immunoprecipitation with ERRα (IP: ERRα; right) are shown, indicating the formation of protein complexes between ERRα and USP14/UCHL5.

3.8. Reduction of mitochondrial biosynthesis mediated ERRα suppression in PDAC

First of all, to confirm the binding activity of ERRα to ERRE by b-AP15, a luciferase assay was performed using a 3X ERRE-luciferase plasmid (Fig. 14A). ERRE is the binding motif site of ERRα, the sequence of which is TCAAGGTCA. The PDAC cells transfected with this luciferase plasmid could be estimate as the binding activity of ERRα by luciferase assay. The luciferase assay reulsts revealed that b-AP15 treatment with 0.0 uM, 0.5 uM and 1.0 uM in PANC1 and MIAPACA2 showed a dose-dependent decreased luciferase activity (Fig. 14B). The results demonstrated that binding activity of ERRα to ERRE was diminished, which could be interpreted as a decrease in the expression of ERRα target genes.

To identify the target genes of ERRα, ERRα-ChIP-seq data of GSE163166[66] from GEO was employed. GSE163166 data, consisting of ERRα and input samples, was utilized to identify specific target genes of ERRα in MDA-MB-231 cells, a breast cancer cell line. The analysis was performed on UCSC genome browser and the location of ERRE was identified using JASPAR CORE 2024. The ChIP-seq analysis demonstrated that the ERRE (yellow) located in the highest peaks (red) near the respiratocy complex genes (blue) including NDUFA2, SDHA, COX8A, NDUFS7, NDUFS5, NDUFV2, COX6B1, and ATP5PO (Fig. 14C, 15A). Given the mitochondrial biosynthesis function of ERRa and the overlaps of the highest peaks with ERRE, it was anticipated that the reduction in the binding activity of ERRa to ERRE could influence the expression of these genes. Among them, three respiratory complex 1 to 3 genes, NDUFA2, SDHA and COX8A, were employed in the ChIP assay.

A statistically significant reduction of expression levels was observed for NDUFA2, SDHA and COX8A in the b-AP15 group compared to the control group in PDAC (Fig. 14C). To demonstrate the decrease in target gene expression due to decreased binding ERRE of ERRα, the ERRα-ChIP assay in MIAPACA2 was performed. The primers for the ChIP-qPCR were designed to capture the highest peak and the sequnce containing the ERRE. ERRα-ChIP-qPCR results presented that targeting the ERRE sequences using the primers were higher in ERRα samples compared to IgG samples, indicating that the ERRα-ChIP was successful. Subsequently, the results demonstrated that the ERRE near NDUFA2 (p = 0.0003), SDHA (p = 0.0064) and COX8A (p = 0.0036) were significantly diminished in the b-AP15 group compared to the control group. The results of this study showed that USP14 and UCHL5 supression reduced ERRE binding activity of ERRα,

resulting in significant downregulation of ERRα target genes expression.

To confirm the reduction in mitochondrial biosynthesis, mtDNA assessment was performed. It was estimated by extracting total genomic DNA from PDAC cells and normalizing of mtDNA relative to nDNA. Cytochrome b/CYTB, a representative of mtDNA, is one of the components of the respiratory chain complex 3, and β2 microglobulin/B2M, a representative of nDNA, is one of the histocompatibility complex (MHC) class I components. The mtDNA/nDNA ratio results demonstrated a statistically significant reduction in the b-AP15 group relative to the control group in both cell types (Fig. 16A).

Subsequently, ICC was performed to identify mitochondrial copy changes caused by decreased mitochondrial biosynthesis. The nuclei were stained with Hoechst33342 (blue) and the mitochondria were stained with Mitotracker (red) (Fig. 16B). The two stained images were merged to present the overall stain appearance of the cell. The b-AP15 group exhibited diminished mitochondrial staining in both PANC1 and MIAPACA2 cells relative to the control group. To quantify the mitochondria stain, its intensity was measured and results demonstrated that both PANC1 ($p < 0.0001$) and MIAPACA2 ($p < 0.0001$) were significantly reduced by about half in the b-AP15 group compared to control group (Fig. 16C). These data suggest that USP14 and UCHL5 inhibition suppressed the mitochondrial biosynthesis by reducing the binding activity of ERRα to ERRE.

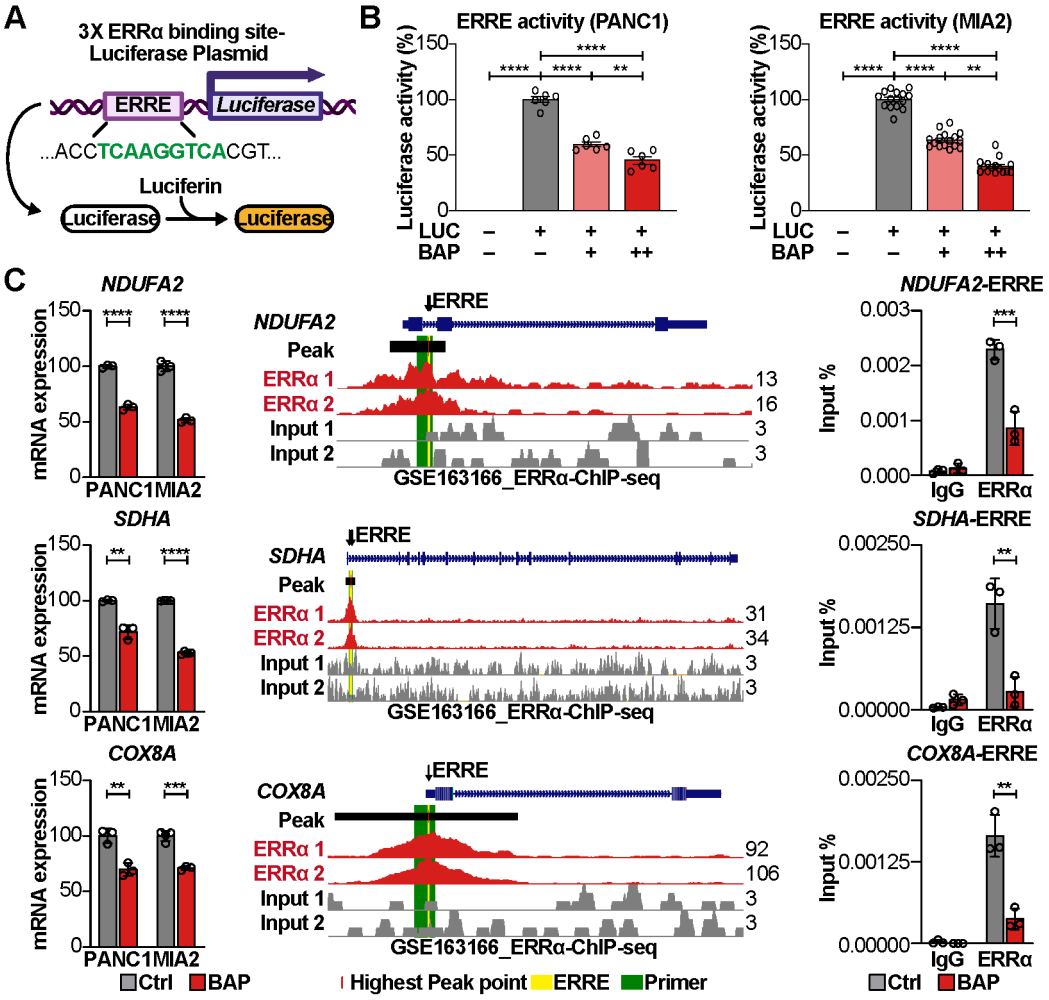

Figure 14. ChIP assay presenting decreased ERRα binding activity to ERRE by USP14 and UCHL5 inhibition. (A) Luciferase plasmid containing 3X ERRE promoter assessing binding activity of ERRα to ERRE in transfected cells. (B) Luciferase assay presenting comparison of ERRE activity n PANC1 and MIAPACA2 cells treated with b-AP15. Bar graphs presenting changes in binding activity upon treatment with 0.5 μM and 1.0 μM b-AP15. (C) mRNA epression levels in control and b-AP15 groups (left pannel), ERRα-ChIP-seq analysis using GSE163166 (middle pannel) and ERRα-ChIP-qPCR in control and b-AP15 groups (right pannel) of respiratory complex genes, NDUFA2, SDHA and COX8A. For Chip-seq analysis, the highest peaks were indicated in red,

ERRE were highlighted in yellow, and qPCR primer regions were shown in green. * $p < 0.05$, ** $p < 0.01$, *** $p < 0.001$, **** $p < 0.0001$.

A

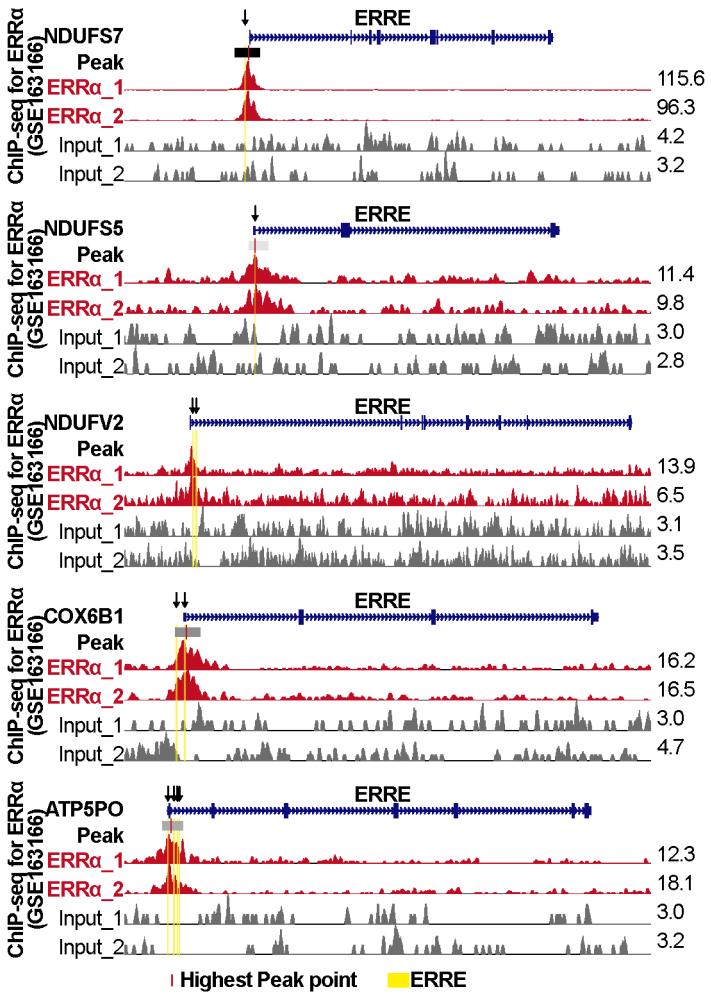

Figure 15. ChIP analysis presenting ERRα binding ERRE near respiratory complex gene. (A) Additional ERRα-ChIP-seq analysis using GSE163166 presenting near the respiratory complex genes, NDUFS7, NDUFS5, NDUFV2, COX6B1, and ATP5PO, exhibited the presence of ERRE as the highest peak of ERRα. The highest peaks were indicated in red and ERRE were highlighted in yellow.

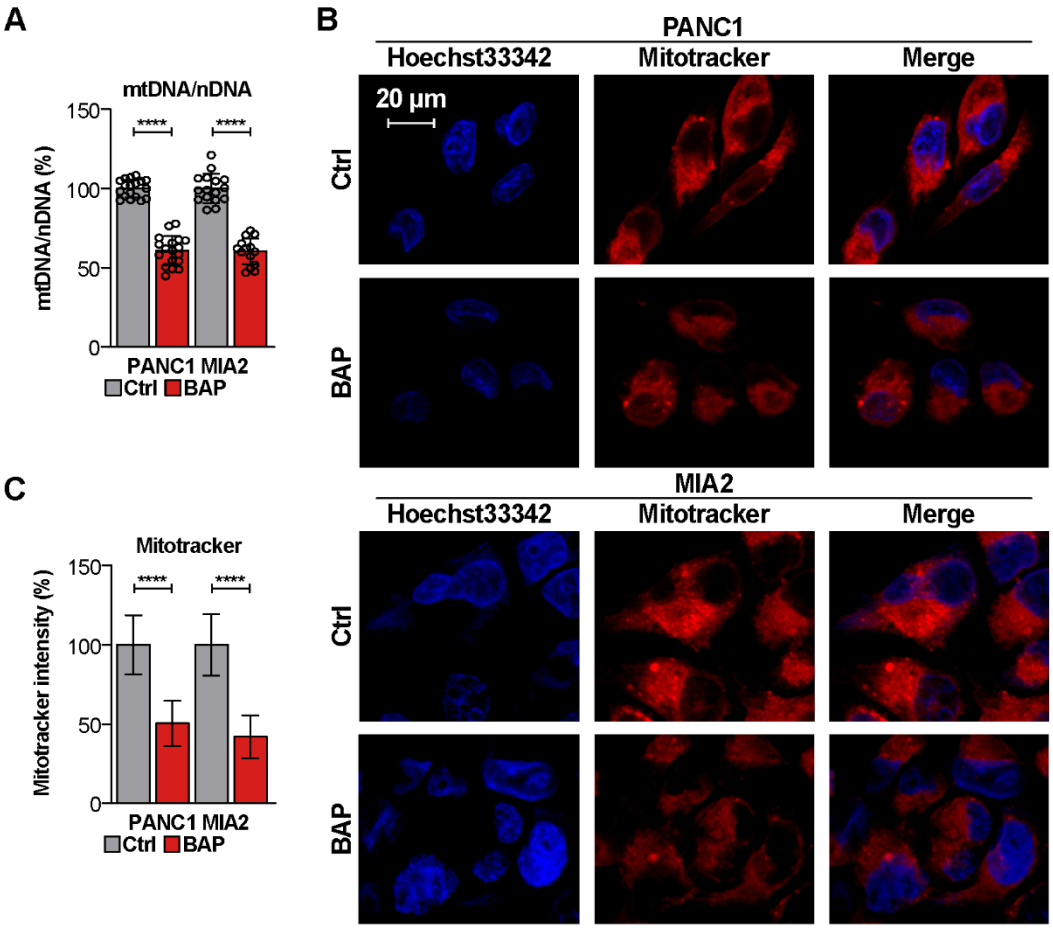

Figure 16. Suppression of mitochondria biosynthesis via USP14 and UCHL5 inhibition. (A) Comparison of mtDNA/nDNA ratio between control and b-AP15 groups in PANC1 and MIAPACA2. (B) ICC staining nuclear (Hoechst33342; blue) and mitochondria (Mitotracker; red) using. The images were taken with a fluorescence microscope. (C) Quantification of mitochondria illustrating the intensity of Mitotracker in control and b-AP15 groups in PDAC. * $p < 0.05$, ** $p < 0.01$, *** $p < 0.001$, **** $p < 0.0001$.

3.9. OXPHOS repression mediated by USP14 and UCHL5 inhibition

To demonstrate that USP14 and UCHL5 inhibition mediated decrease in mitochondrial biosynthesis resulted in a phenotype with abnormal OXPHOS, the oxygen consumption rate (OCR) via XF analysis was performed. The assessed OCR serves as an indicator of mitochondrial function, which can be utilized for the estimation of OXPHOS. To reduce the oxygen consumption rate (OCR), 2 μM oligomycin and 1 μM rotenone/antimycin A (R/A), which inhibit respiratory complex 5 and 1/3, were employed. Additionally, 2 μM carbonyl cyanide-p-trifluoromethoxyphenylhydrazone (FCCP), uncoupling agent inducing maximum OCR, was employed. From this XF analysis, basal respiration, maximal respiration, spare respiratory capacity and ATP production parameters were obtained.

The XF assay results showed an overall trend of siginificantly decreased OCR in the b-AP15 group compared to control group (Fig. 17A). The basal OCR was found to be significantly reduced, as were its maximal respiration and spare respiratory capacity (Fig. 17B). This resulted in a reduction in ATP production, which is the primary function of the mitochondria and the electron transport chain. Moreover, the reduction in estimated ATP production was corroborated by cellular ATP ratio measurements (Fig. 17C). These findings revealed that mitochondrial dysfunction was induced by inhibition of USP14 and UCHL5, critically reducing cellular energy sources.

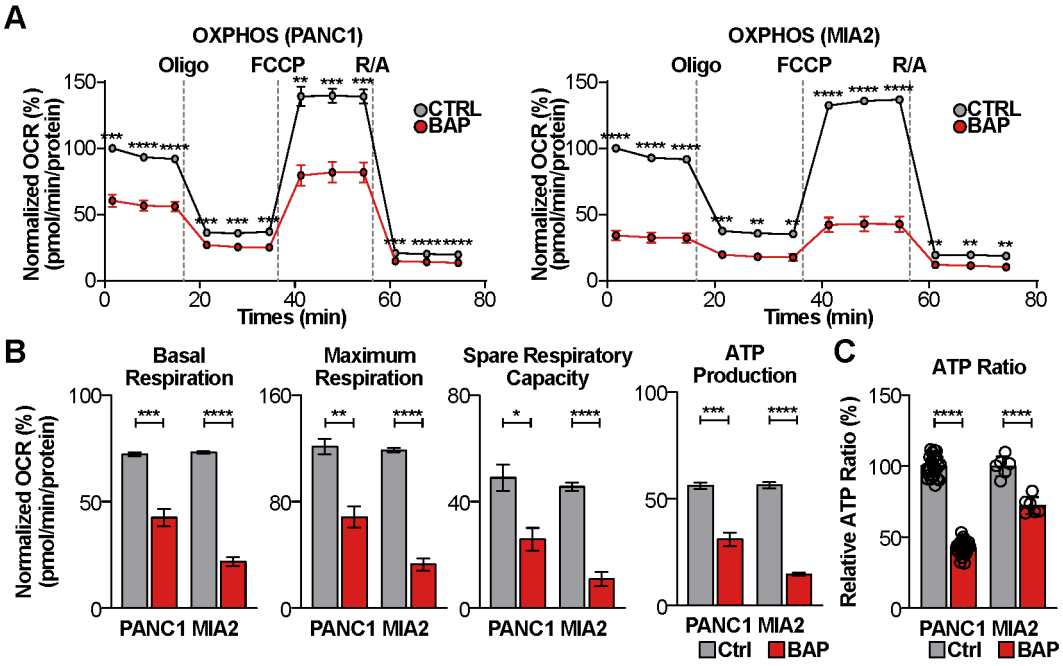

Figure 17. OXPHOS repression induced by USP14 and UCHL5 inhibition. (A) OCR comparing control and b-AP15 groups in PDAC cells upon response to Oligomycin, FCCP and Rotenone/antimycin A (R/A). Oligomycin is the respiratory complex 5 inhibitor, FCCP is the uncoupling agent, and R/A is the respiratory complex 1 and 3 inhibitor. (B) The estimation of several mitochondrial parameters, including basal respiration, maximum respiration, spare respiratory capacity, and ATP production, conducted using OCR data presenting mitochondrial dysfunction in the b-AP15 group. (C) The cellular ATP ratio between the control and b-AP15 groups showing evidence of a direct decrease in energy production. * $p < 0.05$, ** $p < 0.01$, *** $p < 0.001$, **** $p < 0.0001$.

4. DISCUSSION

Here this study demonstrated that the proteasomal deubiquitinases, USP14 and UCHL5, were overexpressed in pancreatic ductal cells in PDAC. Targeting these proteins with b-AP15 induced proteotoxic and oxidative stress, while simultaneously disrupting cancer cell proliferation and mitochondrial function through autophagic degradation of ERRα. The above findings suggested that inhibition of USP14 and UCHL5 is novel therapeutic target for PDAC.

PDAC remains a formidable challenge due to its aggressiveness and resistance issuess of regimen. Despite advances in understanding of PDAC, the 5-year survival rate of PDAC patients is still very poor. There is a fully unmet need for cancer cell-specific and effective targets for PDAC. Therefore, variable target genes for therapeutic strategies are currently under investigation, with numerous findings emerging from scRNA-seq analysis in recent years. The published sequencing data were employed in this dissertation to find out the clinical implication of USP14 and UCHL5.

My initial hypothesis, that USP14 and UCHL5 expression levels are elevated in PDAC, was validated by spatial scRNA-seq analysis and IHC assay. Moreover, increased expression levels of USP14 and UCHL5 were observed in aggressive ductal cells, as identified through the pseudotime using scRNA-seq analysis. Given that USP14 and UCHL5 expression were correlated to poor survival rate in PDAC patients, this study concentrated on USP14 and UCHL5 as potential novel therapeutic targets for aggressive ductal cells in PDAC.

First of all, in vitro and in vivo experiments using b-AP15 were performed. The proliferation of PDAC cell lines, PANC1 and MIAPACA2, were suppressed in the b-AP15 group compared to the control group. The supplementary results of the colony formation and wound healing assays indicated that efficacy of b-AP15 in PDAC cell lines. In vivo xenograft assay demonstrated that b-AP15 significantly inhibited tumor growth in xenograft models, demonstrated the efficacy of b-AP15 on even in vivo research.

To research the proliferation suppression mechanism of b-AP15, the LC/MS and bulk RNA-seq analysis were conducted. The calculated protein and RNA expression levels were facilitated as the investigation of the cellular phenotypic changes induced by b-AP15. The GSEA results showed that there were two main phenotypic changes, UPR and OXPHOS. b-AP15 treatment inhibited the function of the 19S regulatory particles of the proteasome, preventing proteasomal degradation. This proteotoxic stress resulted in oxidative stress, including ROS, and cellular impairment of the redox system. The increased process from superoxide to ROS and the decreased ability of glutathione to

reduce ROS eventually led to the accumulation of ROS in the cell, ultimately leading to the oxidized protein accumulation.

Concurrently, the significant diminishment of OXPHOS, a marker of mitochondrial function, was driven by b-AP15. In particular, the decrease in motif activity of ERRα, which is involved in mitochondrial biosynthesis, was observed in bulk RNA-seq analysis. The most interesting point was ERRα expression pattern at the protein and RNA levels. The impact of b-AP15 on RNA expression levels was unaltered, whereas a critical reduction in protein expression was observed. The reduction of protein expression was found to be both dose- and time-dependent in b-AP15 treatment, suggesting that the protein were processed degradation following RNA translation. My first experimental hypothesis was that the degradation of ERRα was due to proteasomal degradation, given that proteasomal degradation is directly affected by the 20S core particle. However, MG132, a proteasome inhibitor, did not affect any protein expression levels of ERRα. Subsequently, given that huge proteotoxic stress was induced by b-AP15 treatement, bafilomycin A1, the inhibitor for autophagic degradation, was employed. Importantly, the autophagy inhibition prevented ERRα degradation by b-AP15. These findings revealed that the degradation of ERRα was caused by autophagic degradation. Furthermore, it constituted a crucial element in elucidating the observed decline in OXPHOS.

The activation of ERRα is contingent upon its binding to the ERRE binding motif site. Therefore, an ERRE-luciferase plasmid was employed to simulate the ERRE binding activity of ERRα. As expected, the results showed that the ERRE binding activity of ERRα was reduced in b-AP15 group, as evidenced by a reduction in luciferase activity. To predict which gene expression is affected by ERRα, the exact locations of the ERRE near the predicted genes were identified through a publicly available ERRα-ChIP-seq analysis. The respiratory complex genes, NDUFA2, SDHA, COX8A, and others exhibited the highest ERRα ChIP peaks. Importantly, these peaks were located within ERRE. To confirm it, I performed ChIP using an ERRα specific antibody and obtained samples for the control and b-AP15 groups. ChIP-qPCR revealed that the ERRE peak signals near the predicted genes were down-regulated by b-AP15, suggesting that the decreased activity of ERRα affected the expression of the predicted respiratory complex genes. In addition, the inhibition of USP14 and UCHL5 led to a decrease in the mtDNA/nDNA ratio and a reduction in mitochondrial copies. The subsequent OXPHOS assay results were significantly reduced in the b-AP15 group, with multiple parameters indicating overall mitochondrial dysfunction.

While this study provided valuable insights into the underlying mechanisms of b-AP15, further investigations are necessary to explore the combinatorial effects of b-AP15 with existing anti-PDAC agents, gemcitabine and paclitaxel. A recently published paper presented an intriguing finding that gemcitabine resistance in pancreatic cancer cell lines, PANC1 and MIAPACA2, was associated with enhanced mitochondrial function[67]. In addition, other research also demonstrated that gemcitabine-resistant MIAPACA2 exhibited higher OCR than control cell[68]. In patients resistant to the first line anti-cancer agent gemcitabine, targeting USP14 and UCHL5 might also serve as a therapeutic strategy for resistant cancer cells through inducing mitochondrial dysfunction.

Collectively, these findings revealed the novel mechanisms of b-AP15 on PDAC. By inducing proteotoxic stress and targeting ERRα for autophagic degradation, b-AP15 effectively suppressed PDAC cell proliferation and tumor growth. These results highlighted the therapeutic potential of targeting USP14 and UCHL5 as a PDAC therapeutic strategy.

5. CONCLUSION

This study demonstrates that USP14 and UCHL5, overexpressed in pancreatic ductal cancer cells, are correlated to survival rate of PDAC patients. By inhibiting USP14 and UCHL5 with b-AP15, I demonstrated significant suppression of PDAC cell growth and tumor development. Mechanistically, b-AP15 induces proteotoxic and oxidative stress, leading to mitochondrial dysfunction through ERRα degradation. These findings highlight the therapeutic potential of targeting USP14 and UCHL5 for PDAC treatment.

References

1. Siegel, R. L., Giaquinto, A. N., & Jemal, A. (2024). Cancer statistics, 2024. *CA Cancer J Clin, 74*(1), 12-49.
2. Rahib, L., Smith, B. D., Aizenberg, R., Rosenzweig, A. B., Fleshman, J. M., & Matrisian, L. M. (2014). Projecting cancer incidence and deaths to 2030: the unexpected burden of thyroid, liver, and pancreas cancers in the United States. *Cancer Res, 74*(11), 2913-2921.
3. Pishvaian, M. J., & Brody, J. R. (2017). Therapeutic Implications of Molecular Subtyping for Pancreatic Cancer. *Oncology (Williston Park), 31*(3), 159-166, 168.
4. Sarantis, P., Koustas, E., Papadimitropoulou, A., Papavassiliou, A. G., & Karamouzis, M. V. (2020). Pancreatic ductal adenocarcinoma: Treatment hurdles, tumor microenvironment and immunotherapy. *World J Gastrointest Oncol, 12*(2), 173-181.
5. Feldmann, G., Rauenzahn, S., & Maitra, A. (2009). In vitro models of pancreatic cancer for translational oncology research. *Expert Opin Drug Discov, 4*(4), 429-443.
6. Wood, L. D., & Hruban, R. H. (2012). Pathology and molecular genetics of pancreatic neoplasms. *Cancer J, 18*(6), 492-501.
7. Vogelstein, B., Papadopoulos, N., Velculescu, V. E., Zhou, S., Diaz, L. A., Jr., & Kinzler, K. W. (2013). Cancer genome landscapes. *science, 339*(6127), 1546-1558.
8. Kamisawa, T., Wood, L. D., Itoi, T., & Takaori, K. (2016). Pancreatic cancer. *Lancet, 388*(10039), 73-85.
9. Hanahan, D., & Weinberg, R. A. (2011). Hallmarks of cancer: the next generation. *Cell, 144*(5), 646-674.
10. Schmidt, C. M., Powell, E. S., Yiannoutsos, C. T., Howard, T. J., Wiebke, E. A., Wiesenauer, C. A., . . . Madura, J. A. (2004). Pancreaticoduodenectomy: a 20-year experience in 516 patients. *Arch Surg, 139*(7), 718-725; discussion 725-717.
11. Hall, W. A., & Goodman, K. A. (2019). Radiation therapy for pancreatic adenocarcinoma, a treatment option that must be considered in the management of a devastating malignancy. *Radiation Oncology, 14*, 1-5.
12. Principe, D. R., Underwood, P. W., Korc, M., Trevino, J. G., Munshi, H. G., & Rana, A. (2021). The Current Treatment Paradigm for Pancreatic Ductal Adenocarcinoma and Barriers to Therapeutic Efficacy. *Front Oncol, 11*, 688377.

13. Zeng, S., Pottler, M., Lan, B., Grutzmann, R., Pilarsky, C., & Yang, H. (2019). Chemoresistance in Pancreatic Cancer. *Int J Mol Sci, 20*(18), 4504.
14. Swatek, K. N., & Komander, D. (2016). Ubiquitin modifications. *Cell Res, 26*(4), 399-422.
15. Bard, J. A. M., Goodall, E. A., Greene, E. R., Jonsson, E., Dong, K. C., & Martin, A. (2018). Structure and Function of the 26S Proteasome. *Annu Rev Biochem, 87*(1), 697-724.
16. Lee, M. J., Lee, B.-H., Hanna, J., King, R. W., & Finley, D. (2011). Trimming of ubiquitin chains by proteasome-associated deubiquitinating enzymes. *Molecular & Cellular Proteomics, 10*(5).
17. Hamazaki, J., Iemura, S., Natsume, T., Yashiroda, H., Tanaka, K., & Murata, S. (2006). A novel proteasome interacting protein recruits the deubiquitinating enzyme UCH37 to 26S proteasomes. *EMBO J, 25*(19), 4524-4536.
18. Lee, B. H., Lu, Y., Prado, M. A., Shi, Y., Tian, G., Sun, S. W., . . . Finley, D. (2016). USP14 deubiquitinates proteasome-bound substrates that are ubiquitinated at multiple sites. *Nature, 532*(7599), 398-+.
19. Hipp, M. S., Kasturi, P., & Hartl, F. U. (2019). The proteostasis network and its decline in ageing. *Nat Rev Mol Cell Biol, 20*(7), 421-435.
20. Deshaies, R. J. (2014). Proteotoxic crisis, the ubiquitin-proteasome system, and cancer therapy. *BMC Biol, 12*, 94.
21. Tsvetkov, P., Adler, J., Myers, N., Biran, A., Reuven, N., & Shaul, Y. (2018). Oncogenic addiction to high 26S proteasome level. *Cell Death Dis, 9*(7), 773.
22. Solimini, N. L., Luo, J., & Elledge, S. J. (2007). Non-oncogene addiction and the stress phenotype of cancer cells. *Cell, 130*(6), 986-988.
23. Richardson, P. G., Barlogie, B., Berenson, J., Singhal, S., Jagannath, S., Irwin, D., . . . Anderson, K. C. (2003). A phase 2 study of bortezomib in relapsed, refractory myeloma. *N Engl J Med, 348*(26), 2609-2617.
24. Siegel, D. S., Martin, T., Wang, M., Vij, R., Jakubowiak, A. J., Lonial, S., . . . Jagannath, S. (2012). A phase 2 study of single-agent carfilzomib (PX-171-003-A1) in patients with relapsed and refractory multiple myeloma. *Blood, 120*(14), 2817-2825.
25. Gentile, M., Offidani, M., Vigna, E., Corvatta, L., Recchia, A. G., Morabito, L., . . . Gentili, S. (2015). Ixazomib for the treatment of multiple myeloma. *Expert Opin Investig Drugs, 24*(9), 1287-1298.

26. Kozuch, P. S., Rocha-Lima, C. M., Dragovich, T., Hochster, H., O'Neil, B. H., Atiq, O. T., . . . Lenz, H. J. (2008). Bortezomib with or without irinotecan in relapsed or refractory colorectal cancer: Results from a randomized phase II study. *Journal of clinical oncology, 26*(14), 2320-2326.

27. Jatoi, A., Dakhil, S. R., Foster, N. R., Ma, C., Rowland, K. M., Moore, D. F., . . . Alberts, S. R. (2008). Bortezomib, paclitaxel, and carboplatin as a first-line regimen for patients with metastatic esophageal, gastric, and gastroesophageal cancer - Phase II Results from the North Central Cancer Treatment Group (N044B). *Journal of thoracic oncology, 3*(5), 516-520.

28. Hainsworth, J. D., Meluch, A. A., Spigel, D. R., Barton, J., Simons, L., Meng, C., . . . Greco, E. A. (2007). Weekly docetaxel and bortezomib as first-line treatment for patients with hormone-refractory prostate cancer: A minnie pearl cancer research network phase II trial. *Clinical genitourinary cancer, 5*(4), 278-283.

29. Ramalingam, S. S., Davies, A. M., Longmate, J., Edelman, M. J., Lara, P. N., Jr., Vokes, E. E., . . . Gandara, D. R. (2011). Bortezomib for patients with advanced-stage bronchioloalveolar carcinoma: a California Cancer Consortium Phase II study (NCI 7003). *J Thorac Oncol, 6*(10), 1741-1745.

30. Furuyama, T., Tanaka, S., Shimada, S., Akiyama, Y., Matsumura, S., Mitsunori, Y., . . . Tanabe, M. (2016). Proteasome activity is required for the initiation of precancerous pancreatic lesions. *Scientific reports, 6*(1), 27044.

31. Liu, Y., Deguchi, Y., Wei, D., Liu, F., Moussalli, M. J., Deguchi, E., . . . Shureiqi, I. (2022). Rapid acceleration of KRAS-mutant pancreatic carcinogenesis via remodeling of tumor immune microenvironment by PPARdelta. *Nat Commun, 13*(1), 2665.

32. D'Arcy, P., Brnjic, S., Olofsson, M. H., Fryknäs, M., Lindsten, K., De Cesare, M., . . . Linder, S. (2011). Inhibition of proteasome deubiquitinating activity as a new cancer therapy. *Nature medicine, 17*(12), 1636-U1150.

33. D'arcy, P., Brnjic, S., Olofsson, M. H., Fryknäs, M., Lindsten, K., De Cesare, M., . . . Larsson, R. (2011). Inhibition of proteasome deubiquitinating activity as a new cancer therapy. *Nature medicine, 17*(12), 1636-1640.

34. Oh, Y.-T., Deng, L., Deng, J., & Sun, S.-Y. (2017). The proteasome deubiquitinase inhibitor b-AP15 enhances DR5 activation-induced apoptosis through stabilizing DR5. *Scientific*

reports, 7(1), 8027.

35. Jiang, L., Sun, Y., Wang, J., He, Q., Chen, X., Lan, X., . . . Liu, J. (2019). Proteasomal cysteine deubiquitinase inhibitor b-AP15 suppresses migration and induces apoptosis in diffuse large B cell lymphoma. *Journal of Experimental & Clinical Cancer Research, 38*(1), 1-14.
36. Feng, X., Holmlund, T., Zheng, C., & Fadeel, B. (2014). Proapoptotic effects of the novel proteasome inhibitor b-AP15 on multiple myeloma cells and natural killer cells. *Experimental hematology, 42*(3), 172-182.
37. Mirebeau-Prunier, D., Le Pennec, S., Jacques, C., Gueguen, N., Poirier, J., Malthiery, Y., & Savagner, F. (2010). Estrogen-related receptor alpha and PGC-1-related coactivator constitute a novel complex mediating the biogenesis of functional mitochondria. *FEBS J, 277*(3), 713-725.
38. Schreiber, S. N., Emter, R., Hock, M. B., Knutti, D., Cardenas, J., Podvinec, M., . . . Kralli, A. (2004). The estrogen-related receptor alpha (ERRalpha) functions in PPARgamma coactivator 1alpha (PGC-1alpha)-induced mitochondrial biogenesis. *Proc Natl Acad Sci U S A, 101*(17), 6472-6477.
39. Mootha, V. K., Handschin, C., Arlow, D., Xie, X. H., St Pierre, J., Sihag, S., . . . Spiegelman, B. M. (2004). Errα and Gabpa/b specify PGC-1α-dependent oxidative phosphorylation gene expression that is altered in diabetic muscle. *Proceedings of the National Academy of Sciences of the United States of America, 101*(17), 6570-6575.
40. Tang, Z., Li, C., Kang, B., Gao, G., Li, C., & Zhang, Z. (2017). GEPIA: a web server for cancer and normal gene expression profiling and interactive analyses. *Nucleic acids research, 45*(W1), W98-W102.
41. Al-Kafaji, G., & Golbahar, J. (2013). High glucose-induced oxidative stress increases the copy number of mitochondrial DNA in human mesangial cells. *Biomed Res Int, 2013*(1), 754946.
42. Espinet, E., Klein, L., Puré, E., & Singh, S. K. (2022). Mechanisms of PDAC subtype heterogeneity and therapy response. *Trends in Cancer, 8*(12), 1060-1071.
43. Shinkawa, T., Ohuchida, K., Mochida, Y., Sakihama, K., Iwamoto, C., Abe, T., . . . Ikenaga, N. (2022). Subtypes in pancreatic ductal adenocarcinoma based on niche factor dependency show distinct drug treatment responses. *Journal of Experimental & Clinical Cancer*

Research, 41(1), 89.

44. Moffitt, R. A., Marayati, R., Flate, E. L., Volmar, K. E., Loeza, S. G. H., Hoadley, K. A., . . . Chung, A. H. (2015). Virtual microdissection identifies distinct tumor-and stroma-specific subtypes of pancreatic ductal adenocarcinoma. *Nature genetics, 47*(10), 1168-1178.
45. Deer, E. L., González-Hernández, J., Coursen, J. D., Shea, J. E., Ngatia, J., Scaife, C. L., . . . Mulvihill, S. J. (2010). Phenotype and genotype of pancreatic cancer cell lines. *Pancreas, 39*(4), 425-435.
46. Rauluseviciute, I., Riudavets-Puig, R., Blanc-Mathieu, R., Castro-Mondragon, J. A., Ferenc, K., Kumar, V., . . . Baranasic, D. (2024). JASPAR 2024: 20th anniversary of the open-access database of transcription factor binding profiles. *Nucleic acids research, 52*(D1), D174-D182.
47. Haeri, M., & Knox, B. E. (2012). Endoplasmic reticulum stress and unfolded protein response pathways: potential for treating age-related retinal degeneration. *Journal of ophthalmic & vision research, 7*(1), 45.
48. Liu, Z., Lv, Y., Zhao, N., Guan, G., & Wang, J. (2015). Protein kinase R-like ER kinase and its role in endoplasmic reticulum stress-decided cell fate. *Cell death & disease, 6*(7), e1822-e1822.
49. Shi, Z., Yu, X., Yuan, M., Lv, W., Feng, T., Bai, R., & Zhong, H. (2019). Activation of the PERK-ATF4 pathway promotes chemo-resistance in colon cancer cells. *Scientific reports, 9*(1), 3210.
50. Wang, L., Liu, Y., Du, T., Yang, H., Lei, L., Guo, M., . . . Chen, X. (2020). ATF3 promotes erastin-induced ferroptosis by suppressing system Xc–. *Cell Death & Differentiation, 27*(2), 662-675.
51. Cao, S. S., & Kaufman, R. J. (2014). Endoplasmic reticulum stress and oxidative stress in cell fate decision and human disease. *Antioxidants & redox signaling, 21*(3), 396-413.
52. Chong, W. C., Shastri, M. D., & Eri, R. (2017). Endoplasmic reticulum stress and oxidative stress: a vicious nexus implicated in bowel disease pathophysiology. *International journal of molecular sciences, 18*(4), 771.
53. Ong, G., & Logue, S. E. (2023). Unfolding the interactions between endoplasmic reticulum stress and oxidative stress. *Antioxidants, 12*(5), 981.
54. Bhattarai, K. R., Riaz, T. A., Kim, H.-R., & Chae, H.-J. (2021). The aftermath of the

interplay between the endoplasmic reticulum stress response and redox signaling. *Experimental & molecular medicine, 53*(2), 151-167.

55. Wang, Y., Branicky, R., Noë, A., & Hekimi, S. (2018). Superoxide dismutases: Dual roles in controlling ROS damage and regulating ROS signaling. *Journal of Cell Biology, 217*(6), 1915-1928.
56. Chiang, S.-K., Chen, S.-E., & Chang, L.-C. (2021). The role of HO-1 and its crosstalk with oxidative stress in cancer cell survival. *Cells, 10*(9), 2401.
57. Ryter, S. W., & Choi, A. M. (2005). Heme oxygenase-1: redox regulation of a stress protein in lung and cell culture models. *Antioxidants & redox signaling, 7*(1-2), 80-91.
58. Zhang, H., & Forman, H. J. (2012). *Glutathione synthesis and its role in redox signaling.* Paper presented at the Seminars in cell & developmental biology.
59. Aquilano, K., Baldelli, S., & Ciriolo, M. R. (2014). Glutathione: new roles in redox signaling for an old antioxidant. *Frontiers in pharmacology, 5*, 196.
60. Sitte, N., Merker, K., von Zglinicki, T., & Grune, T. (2000). Protein oxidation and degradation during proliferative senescence of human MRC-5 fibroblasts. *Free Radical Biology and Medicine, 28*(5), 701-708.
61. Reeg, S., & Grune, T. (2015). Protein oxidation in aging: does it play a role in aging progression? *Antioxidants & redox signaling, 23*(3), 239-255.
62. Kim, Y. M., & Kim, H.-J. (2020). Proteasome inhibitor MG132 is toxic and inhibits the proliferation of rat neural stem cells but increases BDNF expression to protect neurons. *Biomolecules, 10*(11), 1507.
63. Wang, D., Xu, Q., Yuan, Q., Jia, M., Niu, H., Liu, X., . . . Yuan, H. (2019). Proteasome inhibition boosts autophagic degradation of ubiquitinated-AGR2 and enhances the antitumor efficiency of bevacizumab. *Oncogene, 38*(18), 3458-3474.
64. Wang, R., Wang, J., Hassan, A., Lee, C.-H., Xie, X.-S., & Li, X. (2021). Molecular basis of V-ATPase inhibition by bafilomycin A1. *Nature communications, 12*(1), 1782.
65. Mauvezin, C., & Neufeld, T. P. (2015). Bafilomycin A1 disrupts autophagic flux by inhibiting both V-ATPase-dependent acidification and Ca-P60A/SERCA-dependent autophagosome-lysosome fusion. *Autophagy, 11*(8), 1437-1438.
66. Cerutti, C., Zhang, L., Tribollet, V., Shi, J.-R., Brillet, R., Gillet, B., . . . Vanacker, J.-M. (2022). Computational identification of new potential transcriptional partners of ERRα in

breast cancer cells: specific partners for specific targets. *Scientific reports, 12*(1), 3826.

67. Masuo, H., Kubota, K., Shimizu, A., Notake, T., Miyazaki, S., Yoshizawa, T., . . . Soejima, Y. (2023). Increased mitochondria are responsible for the acquisition of gemcitabine resistance in pancreatic cancer cell lines. *Cancer Science, 114*(11), 4388-4400.

68. Fujiwara-Tani, R., Sasaki, T., Takagi, T., Mori, S., Kishi, S., Nishiguchi, Y., . . . Kuniyasu, H. (2022). Gemcitabine resistance in pancreatic ductal carcinoma cell lines stems from reprogramming of energy metabolism. *International journal of molecular sciences, 23*(14), 7824.

Abstract in Korean

췌장암에서 USP14과 UCHL5 매개 ERRα 조절에 의한 미토콘드리아 기능 조절의 치료 잠재력

췌장암의 주요 아형인 췌관 선암종은 5년 생존율이 약 10%에 불과한 치명적인 질환이다. 췌관 선암종의 빠른 증식과 대사 특징으로 인해 단백질의 회전율이 증가되고 이로 인해 단백질 독성 스트레스가 증가한다. 높은 프로테아좀 활성은 췌관 선암종의 치료를 위한 유망한 표적이 됩니다. 두 개의 프로테아좀 탈유비퀴틴 효소인 USP14와 UCHL5는 세포내에서 유비퀴틴 조절자로 작용합니다. 흥미롭게도 췌관 선암종의 시퀀싱 데이터들을 분석한 결과 USP14와 UCHL5는 췌관 암세포에서 높게 발현되었으며, 이는 환자 생존율 저하와 상관관계가 있는 것으로 나타났습니다. 이는 추가적인 시퀀싱 분석과 면역조직화학 분석을 통해서도 확인되었습니다.

USP14와 UCHL5를 잠재적 치료 표적으로 삼기 위해 이 연구에서는 USP14와 UCHL5에 대한 특정 이중 억제제인 b-AP15를 처리한 후 췌관 선암종 세포주가 표현형 변화를 보이는 메커니즘을 조사했습니다. 예상대로 b-AP15 치료는 췌관 선암종 세포주와 이종 이식 모델에서도 유의미한 증식 억제 효과를 보여 잠재적인 치료 효능을 시사했습니다. 세포의 빠른 성장에 따른 세포 표현형 변화를 규명하기 위해 전사체 및 단백질체 분석했습니다. 이러한 종합적인 분석 결과, 췌관 선암종 세포의 미토콘드리아 기능에 중대한 영향을 미친다는 사실이 밝혀졌습니다. 중요한 것은 ERRα 활성 조절을 통해 산화적 인산화를 억제하는 것으로 나타났습니다. 이러한 연구 결과는 PDAC 를 표적으로 하는 치료 전략으로서 b-AP15의 잠재력을 시사합니다.

핵심되는 말 : 췌장암, USP14, UCHL5, ERRα, 산화적 인산화